Department of Physics and Astronomy

University of Heidelberg

Master thesis

in Physics

submitted by

Carina da Costa Castanheira

born in Espariz Tábua (Portugal)

2018

Towards multidimensional spectroscopy experiments in the XUV

This Master thesis has been carried out by

Carina da Costa Castanheira

at the

Max-Planck-Institut für Kernphysik

under the supervision of

Herrn Prof. Dr. Thomas Pfeifer

Auf dem Weg zu multidimensionalen Spektroskopie Experimenten im XUV:

In dieser Arbeit wird der im X-MuSIC (X-ray/XUV Multidimensional Spectroscopy and Impulsive Control) Aufbau verwendete 4-Quadranten Spiegel mittels einer interferometrischen Messung charakterisiert. Dabei wurde für die Bestimmung der Stabilität ein HeNe-Laser und für das Ermitteln des zeitlichen Überlapps der jeweiligen Spiegel zueinander der laboreigene Ti:Sa-Laser verwendet. Der in dieser Arbeit untersuchte 4-Quadranten Spiegel ist dabei der Schlüssel zu Vier-Wellen-Misch-Experimenten. Nach der Bestätigung der notwendigen Parameter der zeitlichen Stabilität und der Charakterisierung des zeitlichen Überlapps wurden im Labor erste nicht-kollineare Vier-Wellen-Misch Experimente im extrem ultravioletten (XUV) Spektralbereich in Neon durchgeführt und untersucht. Des Weiteren wurden unter Verwendung des 4-Quadranten Spiegels erstmals Vier-Wellen-Misch Experimente in Neon im XUV am Freien-Elektronen-Laser FLASH in Hamburg durchgeführt. Die durchgeführten Experimente im XUV bestätigen dabei die Einsetzbarkeit des 4-Quadranten Spiegels und dienen als Basis für zukünftige Vier-Wellen-Misch Experimente mit dem X-MuSIC Aufbau.

Towards multidimensional spectroscopy experiments in the XUV:

In this work the home-built four-quadrant split-mirror of the X-MuSIC beamline is characterised by an interferometric measurement. For this purpose the stability was investigated with a HeNe laser and the temporal overlap between the mirrors themselves was determined under the use of the Ti:Sa laser system available in our lab. This four-quadrant mirror setup is the key to future four-wave mixing (FWM) experiments in the extreme ultraviolet (XUV) spectral region. Beginning with analysing stability properties and finding temporal overlap between the mirrors this work continues with the first measurements on NIR-NIR-XUV four-wave mixing in neon in the extreme ultraviolet (XUV) spectral region.
Futhermore the first XUV-only FWM experiments in neon were performed using the four-quadrant mirror in the XUV region at the free-electron laser facility FLASH in Hamburg (Germany).
The carried-out experiments can be seen as a working proof of the four-quadrant split-mirror and as a basis for future progress in four-wave mixing experiments at the X-MuSIC beamline.

Contents

1. Introduction

Nonlinear multidimensional spectroscopy has advanced drastically from early work on nuclear magnetic resonance in the seventies [1] using radio frequencies in nuclear medicine to many applications in the optical regime [2] including photon echoes [3], transient gratings [4] and multidimensional infrared (IR) spectroscopy([5],[6],[7]). The used wavelength of the applied electromagnetic field imposes a restriction on the spatial resolution for structural imaging and the temporal resolution for tracking dynamical evolution.

The first non-collinear multidimensional electronic spectroscopy experiments carried out in this group in the mid-IR spectral range were performed by Zhang et al. [7] based on a four-quadrant mirror concept. This concept opens up the possibility for passively phase-stable two-dimensional (2D) electronic spectroscopy experiments. The advantage of 2D-spectroscopy is the posibility to extract the complete spectral information in amplitude and phase of the characteristic third-order nonlinear response after the excitation of the system with a three-pulse sequence. Multidimensional spectroscopy experiments have the ability to map the correlation between excitations at different frequencies, thereby directly revealing the energy tranfer and quantum state coupling hidden in complex spectra consisting of overlapping lines. Extending ultrafast nonlinear spectroscopy to the extreme ultraviolet (XUV) regime opens up the posibility to probe valence or core excitation dynamics with unprecedented time resolution.

First nonlinear four-wave mixing measurements in neon have been achieved in an earlier work [8] with a collinear setup using high-harmonic generated XUV light, as well as NIR laser pulses. This led to first measurements of the coherent inner shell wave packet of excited states of different orbital quantum numbers, l = s, p, d.

For future progress in four-wave mixing experiments a new experimental setup based on a grazing incidence four-quadrant split-mirror is tested in this work. With this setup first experiments were performed in the XUV with a high-harmonic source and a free-electron laser.

In this work it is tested if the four-quadrant mirror achieves subwavelength stability that is needed to carry out non-collinear multidimensional experiments in the extreme ultraviolet. Subwavelength stability in the XUV spectral region is still a technological challenge since it requires a precision and reproducibility of a few nanometers.
In addition, the first NIR-NIR-XUV four-wave mixing measurements with this new four-quadrant mirror setup were performed in neon as a target gas. These measurements are presented in this work and a first interpretation of the observed effects will be given. Futhermore, first all-XUV four-wave mixing experiments in neon using the FEL at FLASH are outlined in this work.

2. Theoretical background

2.1. Coherence properties of light

2.1.1. Temporal and spatial coherence

Statistical optics is the study of the properties of random light. Randomness in light occurs because of fluctuations of the light source or the medium which it propagates through. Also mechanical vibrations of optics or scattering from rough surfaces may give rise to random fluctuations which distort the optical wavefront. For the stability measurements of the four-quadrant split-mirror it is important to consider if measured fluctuations arise from the light source itself or from the optics it passes through. To quantize the stability, a concept of statistical averaging is used to define a number of non-random waves. An optical wave is described by a wavefunction $u(\mathbf{r},t) = \Re U(\mathbf{r},t)$, where $\Re$ denotes the real part of the complex wavefunction $U(\mathbf{r},t)$. For coherent light the intensity is given by

$$I(\mathbf{r},t) = |U(\mathbf{r},t)|^2, \tag{2.1}$$

while for random light were U($\mathbf{r}$,t) is a random function of time and position the average intensity is defined as

$$I(\mathbf{r},t) = \langle |U(\mathbf{r},t)|^2 \rangle . \tag{2.2}$$

Random fluctuations in time are characterized by a time scale which represents the "memory" of the fluctuation. To quantize this temporal behavior the statistical average called the autocorrelation function was established. It describes the extent to which the wavefunction fluctuates at two instants of time separated by a given time delay τ

$$G(\tau) = \langle U^*(t)U(t+\tau) \rangle , \tag{2.3}$$

or

$$G(\tau) = \lim_{T\to\infty} \frac{1}{2T} \int_{-T}^{T} U^*(t)U(t+\tau)dt. \tag{2.4}$$

The temporal coherence function G(τ) therefore carries the information about the intensity (I=G(0)) and the degree of correlation, also known as the coherence. The coherence can be measured independent of intensity fluctuations by taking the normalized autocorrelation function

$$g(\tau) = \frac{G(\tau)}{G(0)} = \frac{\langle U^*(t)U(t+\tau)\rangle}{\langle U^*(t)U(t)\rangle}. \tag{2.5}$$

For most light sources the maximum value of $|g(\tau)| = 1$ decreases as τ increases. Since $|g(\tau)|$ decreases with time delay, the value at which it decreases down to half its maximum value is defined as the coherence time τ_c:

$$\tau_c = \int_{-\infty}^{\infty} |g(\tau)|^2 d\tau. \tag{2.6}$$

Per definition light is coherent if the coherence length $l_c = c\tau_c$ is much bigger than the sum of all optical path-lenght differences. Another important quantity is the spectral width $\Delta\nu_c$. It is related to the coherence time via

$$\Delta\nu_c = \frac{1}{\tau_c}. \tag{2.7}$$

To consider spatial and temporal fluctiations of the random light field the cross-correlation function of U($\mathbf{r_1}$,t) and U($\mathbf{r_2}$,t) of positions $\mathbf{r_1}$ and $\mathbf{r_2}$ has to be calculated according to:

$$G(\mathbf{r_1}, \mathbf{r_2}, \tau) = \langle U^*(\mathbf{r_1}, t)U(\mathbf{r_2}, t+\tau)\rangle\,. \tag{2.8}$$

The normalized function is known as the complex degree of coherence:

$$g(\mathbf{r_1}, \mathbf{r_2}, \tau) = \frac{G(\mathbf{r_1}, \mathbf{r_2}, \tau)}{\sqrt{I(\mathbf{r_1})I(\mathbf{r_2})}}. \tag{2.9}$$

2.1.2. Interference of partially coherent light

Coherence is given when all partial waves of an electromagnetic wave oscillate in phase. The coherence property enables waves to create stationary interferences. The intensity of two interfering partially coherent light beams U_1 and U_2 passing a

splitting unit (which in this case serves as an autocorrelator or rather a crosscorrelator) and measured on a detector is given by

$$\begin{aligned} I(x_d,\tau) &= \langle |U_1(x_d,t) + U_2(x_d,t+\tau)|^2 \rangle \\ &= I_1 + I_2 + 2\sqrt{I_1 I_2}|g_{12}|cos\phi, \end{aligned} \tag{2.10}$$

where $\phi = arg\{g_{12}\}$ is the phase of g_{12} with the normalized cross-correlation

$$g_{12} = \frac{\langle U_1^* U_2 \rangle}{\sqrt{I_1 I_2}}, \tag{2.11}$$

and x_d being the position in the detector plane. The first two terms in equation (2.10) account for the intensities of the two beams, the third term introduces a sinusoidal modulation pattern. The strength of the interference pattern is measured by the visibility V. Which is also known as modulation depth or contrast:

$$V = \frac{I_{max} - I_{min}}{I_{max} + I_{min}}. \tag{2.12}$$

With I_{max} and I_{min} being the maximum and minimum values of the intensity. Since $\cos\phi$ can only take values between 1 and -1 inserting equation (2.10) in (2.12) leads to

$$V = \frac{2\sqrt{I_1 I_2}}{I_1 + I_2}|g_{12}|\,. \tag{2.13}$$

In the following it is assumed that the light beam is equally separated in two identical copies so that $I_1 = I_2$. This simplifies equation (2.13) to

$$V = |g_{12}|\,. \tag{2.14}$$

If also considering

$$g_{12} = \frac{\langle U_1^* U_2 \rangle}{I_0} = \frac{\langle U^*(t) U(t+\tau) \rangle}{I_0} = g(\tau),$$

(2.10) simplifies to

$$I = 2I[1 + g(\tau)] = 2I_0[1 + |g(\tau)|\cos\phi(\tau)], \tag{2.15}$$

with $\phi(\tau) = \arg\{g(\tau)\}$. This means that the ability of a wave to interfere with a time delayed replica of itself is influenced by its complex degree of temporal coherence at

this time delay τ. Considering a partially coherent wave with $g(\tau) = g_a(\tau)exp(j\omega_0 t)$ and spectral width $\Delta\nu_c = 1/\tau_c$ the measured intensity is given by

$$I = 2I_0[1 + |g_a(\tau)|\, cos(\omega_0\tau + \phi_a(\tau))], \tag{2.16}$$

where $\phi_a(\tau) = arg\{g_a(\tau)\}$. The relation between intensity I and time delay τ is known as an interferogram and is illustrated in figure 2.1. It peaks at temporal overlap ($\tau = 0$) and vanishes for $\tau \gg \tau_c$. Interference only occurs when the optical path difference is smaller than the coherence length.
The quantity $|g(\tau)|$ can be measured by plotting the visibility of the interference pattern as a function of the time delay, while the phase of $g(\tau)$ can be measured by determining the peak positions of the interference pattern.

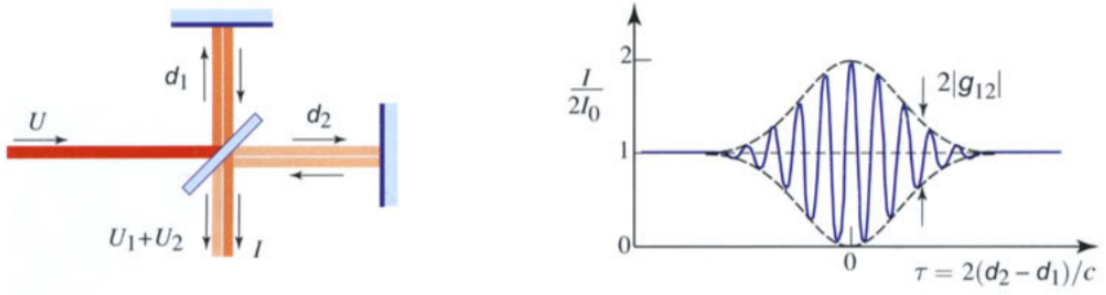

Figure 2.1.: Michelson-interferometer and its resulting normalized intensity $I/2I_0$ as a function of the time delay τ between the pathways d_1 and d_2. This figure is reprinted from [9]

The spectral width of the interfering light source has also an impact on the measured interference. Assuming a wave with a spectral width of $\Delta\nu_c$ centered at ν_0 with $\Delta\nu_c \ll \nu_0$ the complex degree of coherence changes to

$$g(\mathbf{r_1}, \mathbf{r_2}, \tau) = g_a(\mathbf{r_1}, \mathbf{r_2}, \tau)exp(j\omega_0\tau), \tag{2.17}$$

and the intensity is given by

$$I(x) = 2I_0\left[1 + V_x cos\left(\frac{2\pi\theta}{\lambda_0}x + \phi_x\right)\right], \tag{2.18}$$

with $\tau_x = \theta x/c$ and $\lambda_0 = c/\nu_0$. The resulting interference pattern has a sinusoidal course with a period of λ_0/θ with a varying visibility $V_x = \mid g_a(\mathbf{r_1}, \mathbf{r_2}, \tau_x) \mid$ (envelope

of the oscillation) and phase $\phi_x = \arg[g_a(\mathbf{r_1}, \mathbf{r_2}, \tau_x)]$. The interference pattern is in the case of coherent light visible over a distance $x_c = l_c/\theta$, with θ being the angle given by the two pinholes. The angle θ and the center-wavelength $\bar{\lambda}$ of the used light-wave define the distance between the generated interference fringes. It is given by $d_{fringe} = \bar{\lambda}/\theta$. Since the interference pattern is visible over the distance x_c and the fringe spacing is geometrically defined by d_{fringe} is is also possible to determine the number N of visible fringes ($N = l_c/\bar{\lambda} = \nu_0/\Delta\nu_c$). For a spatially non-coherent light source the visibility will be futher reduced and therefore fewer fringes will be observable.

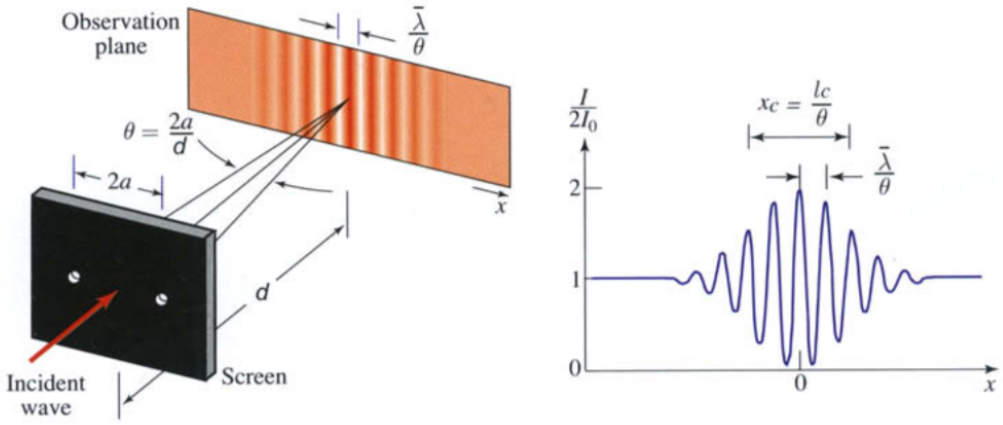

Figure 2.2.: Young's double slit experiment and the created interference fringes as a function of the position x. This figure is reprinted from [9].

2.2. Time resolved spectroscopy in neon

2.2.1. Fano's theory

Spectroscopy gives insight on the internal electronic structure of a system via the absorption line shape of the system. Spectral line shapes are characterized by their energy (E), amplitude (strengh of the process) and spectral width (lifetime Γ). The spectral width is very sensitive and varies with temperature, pressure and phase. Spectral lines which are subject to homogeneous broadening are described by a Lorentzian function.
However if an interaction between several multi-electron-configurations (configuration interaction) is present the shape of the spectral line modifies from a symmetric

Lorentzian profile to an asymmetric Fano profile. These asymmetric resonance line shapes were first observed by Hans Beutler in 1935 [10] and later theoretically described by Ugo Fano [11], [12]. It is based on the interference between quantum transition amplitudes and is predestined for interactions between narrow diskrete states and a broad state, which cold be a continuum or also a short living resonance. Fano's theory parametrizes the line shape with a parameter q that gives a measure for the asymmetry of the resonance line. This parameter q can also be related to the phase of the dipole response of a system [13]. With this mapping the effects experienced by quantum systems upon interaction with ultrashort laser pulses can be investigated via the line-shape change. Considering a bound state $|\alpha\rangle$ and a set of interacting continuum states $|\beta_E\rangle$, the eigenvalues of the Hamiltonian describing this system are

$$\langle\alpha|\hat{H}|\alpha\rangle = E_i, \tag{2.19}$$

$$\langle\beta_E|\hat{H}|\alpha\rangle = V_E, \tag{2.20}$$

$$\langle\beta_E|\hat{H}|\beta_E\rangle = E\delta(E' - E), \tag{2.21}$$

with E_i, E and E' being the energies of the respective states. The off-diagonal elements V_E describe the configuration interaction between the discrete state at energy E_i and a continuum of states with energies E'. Since the ground state has an energy far away from the relevant energies it can be neglected. In order to determine the system's eigenstates the Hamiltonian needs to be diagonalized. The new states are superpositions which are given by [12]:

$$|\Psi\rangle = a_E\,|\alpha\rangle + \int dE' b_{EE'}\,|\beta_E\rangle\,. \tag{2.22}$$

This reduces the problem to the determination of the coefficients a_E and $b_{EE'}$. The complete calculation can be found in [12]. Superposition of different pathways to the continuum leads to quantum-mechanical interference wich results in asymmetric Fano resonance lines. The Fano lines display either constructive or destructive interference depending on the phase between the pathways. The cross section for ionization from the ground state taking quantum path interference into account is given by:

$$\sigma(\epsilon) = \frac{(q+\epsilon)^2}{1+\epsilon^2}, \tag{2.23}$$

with

$$\epsilon = \frac{E - E_i}{\Gamma/2}, \tag{2.24}$$

$$\Gamma = 2\pi V_E^2, \tag{2.25}$$

and

$$q = \frac{\langle \alpha | T | g \rangle}{\pi V_e \langle \beta_E | T | g \rangle}. \tag{2.26}$$

ϵ is the energy expressed in units of the spectral width Γ connencted the finite lifetime of the states. The parameter q represents the ratio between the transitions from the ground to a discrete excited state $|\alpha\rangle$ and the transitions directly to a continuum state $|\beta_E\rangle$. Using the dipole approximation $T \propto d$ the transition matrix elements can be calculated, which leads to:

$$q = \frac{d_{\alpha,g}}{\pi V_E d_{\beta_E,g}}, \tag{2.27}$$

with $d_{\alpha,g}$ and $d_{\beta_E,g}$ being the respective dipole moments. The resulting resonance lines for different values of the q-parameter are plotted in figure 2.3.

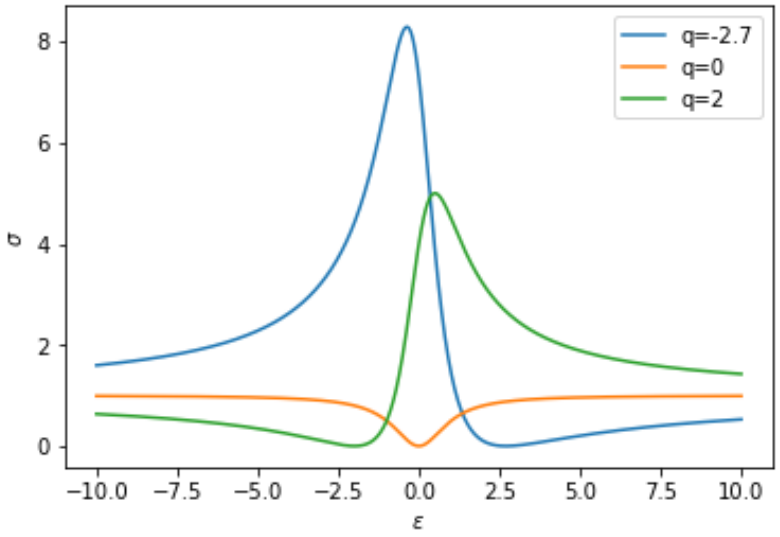

Figure 2.3.: Fano resonance lines plotted for different values of q.

Any resonance can be described by three paramters in the energy domain: the energy E, the linewidth Γ and the line shape parameter q. In [13] it was shown that not only the energy and linewidth but also the q-parameter can be mapped from the energy to the time domain and vice versa by Fourier transformation. The results presented in

[13] show that the time domain representation of q corresponds to a phase offset of the time-dependent dipole response of the system. Regarding the most general form of a dipole response function given by a Dirac delta function and an aditionally exponentially decaying part

$$d(t) \propto c_q \delta(t) + exp\left(-\frac{\Gamma}{2}t + i\left[-Et + \phi(q)\right]\right). \tag{2.28}$$

The Dirac delta function describes a continuum of excited states oscillating at all for the system possible frequencies scaled with c_p. The decaying function describes the dipole emission. The phase offset term $\phi(q)$ describes the phase relative to the one at the moment of excitation. The phase shift and the parameter q are related as follows:

$$\phi(q) = 2\arg(q - i), \quad q(\phi) = -\cot(\tfrac{\phi}{2}). \tag{2.29}$$

This means that if the phase offset can be manipulated the lineshape of a resonance can be tuned.

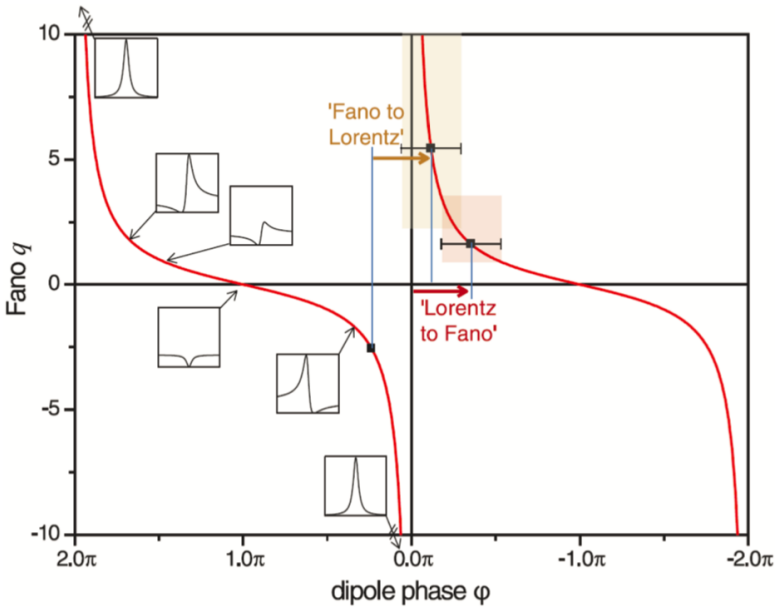

Figure 2.4.: Illustration of the mapping between the Fano parameter q and the dipole phase ϕ. The figure is reprinted from [13].

The phase offset with respect to the Lorentzian line shape can be either induced by configuration interaction or by inducing an additional phase shift of the excited state. This additional phase shift can be easily done by dressing the loosely-bound electron

in the excited state with an ultrashort laser pulse. The states' energy is therefore shifted by the ponderomotive potential

$$\Delta E_p = \frac{e^2 E_0^2}{4m\omega^2}, \tag{2.30}$$

with electron charge e, electron mass m, field strengh E_0 and frequency ω of the laser pulse. During an interation of duration T between the laser pulse and the electron, it aquires an additional phase according to

$$\Delta\phi = \int_0^T \Delta E_p dt. \tag{2.31}$$

Therefore the dipole phase of the system can be changed by either changing the intensity or the temporal duration of interaction.

2.2.2. The neon atom

The noble gas neon is the target system used for the experiments presented in this thesis. First time-resolved experiments on correlated electron dynamics have been performed in this group whith the two-electron system helium [13] where the goal was to excite both electrons at once. Since neon is a few electron system with Z=10 it provides additional correlated-electron excitation modes. Although the higher level of complexity, electron correlation dynamics could be measured on tiniest time scales [14], [15] and theoretically modeled [16], [17] . In the investigated XUV spectral region between 40 and 50 eV the neon atom has doubly excited and 2s innershell excited states. The spectral region is therefore characterized by the Rydberg series of the 2s core-shell excited states and several doubly-excited 2p valence-shell excitations. Both excitation modes lead to quasi-stationary quantum states above the first ionisation threshold ($I_p = 21.56$ eV). These states decay with lifetimes in the femtosecond time scale by electron ejection and electronic rearrangement in the remaining ion.
The neon level sceme with the Rydberg series of the 2s core-shell excited states is presented in 2.5. [Ne] detones therefore the neon atom in its electronic ground state $1s^2 2s^2 2p^8$, while the blue arrow shows the $2s^{-1}3p$ inner-shell transition. The in red depicted states $1s^2 2s 2p^6 3s$ and $1s^2 2s 2p^6 3d$ are dipol-forbidden transitions from the neon gound state [Ne] and therefore dark states for one photon transitions. Since they will play an important role in the later experiment they are additional depicted.

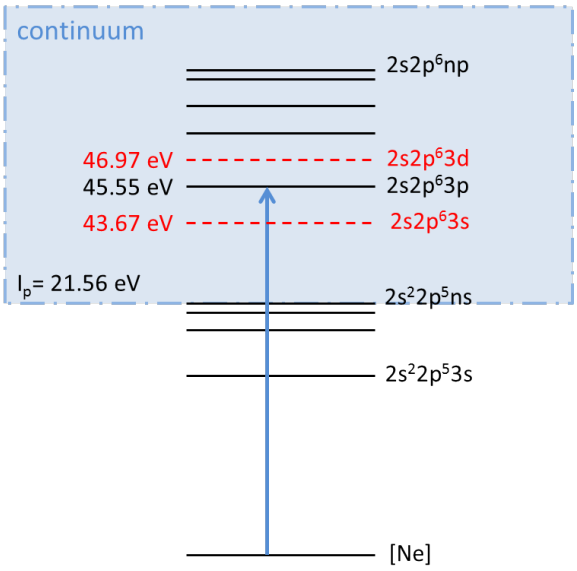

Figure 2.5.: Reduced level sceme of the neon atom with the relevant 2s core-shell excited states. The inner-shell transition $2s^{-1}3p$ (blue arrow) is induced with the use of extreme ultraviolet (XUV) light. The transition leads to quasi-stationary states above the first ionisation threshold ($I_p = 21.56$ eV). These excited states will then decay with lifetimes in the femtosecond time scale by electron ejection and electronic rearrangement in the remaining ion. The in red depicted states $1s^22s2p^63s$ and $1s^22s2p^63d$ are dipol-forbidden transitions from the neon gound state [Ne] and therefore dark states for one photon transitions. Since they will play an important role in the later experiment they are additional depicted.

Since the innershell core excitation process and the direct ionization are competing pathways, the autoionizing states in neon appear as asymmetric Fano lineshapes. In this work dipole allowed states were identified under the use of synchrotron experiments conducted by Codling et al. [18] and Schulz et al. [19], while for dipole forbidden states the electron impact spectroscopy data reported by Min et al. [20] and Spence et al. [21] was consulted.

2.2.3. From linear absorption to four-wave mixing

The advantage of multi-dimensional spectroscopy techniques as for example four-wave mixing (FWM) spectroscopy which is the technique presented in this thesis is that it has the ability to map the correlation between excitations at different frequencies. Thus it is possible to reveal the energy transfer and quantum state coupling between the excitations under investigation. In general multiphoton processes become relevant when high electric field amplitudes are used to excite a system. In this case the relation between electric field and macroscopic polarization

of the medium becomes non-linear.

In linear spectroscopy the polarization $\mathbf{P}(\omega)$ induced by the electric field $\mathbf{E}(\omega)$ is given by

$$\mathbf{P}(\omega) = \epsilon_0 \chi(\omega) \cdot \mathbf{E}(\omega), \tag{2.32}$$

with the dielectric permeability in vacuum ϵ_0 and the dielectric susceptibility $\chi(\omega)$ of the medium. Since the macroscopic dipoles in the medium need some time to align in the oscillating electric field a phase shift between incoming and outgoing (irradiated) electric field is induced. Therefore $\chi(\omega)$ is a complex quantity

$$\chi(\omega) = \chi'(\omega) + i\chi''(\omega), \tag{2.33}$$

which is connected to the refractive index n by the relation

$$n^2 = \epsilon_r = 1 + \chi(\omega). \tag{2.34}$$

The real part of $\chi(\omega)$ accounts for dispersion and the imaginary part accounts for absorption. The absorption of the medium can be described by the absorption coefficient

$$\alpha(\omega) = \frac{\omega}{c} \cdot \chi''(\omega). \tag{2.35}$$

After passing the distance z in the medium the absorption is given by Lambert-Beer's law

$$I(\omega, z) = I_0(\omega) \cdot e^{-\alpha(\omega) z}. \tag{2.36}$$

The macroscopic absorption coefficient $\alpha(\omega)$ and the microscopic atomic cross section $\sigma(\omega)$ are connected via

$$\alpha(\omega) = \rho_N \cdot \sigma(\omega), \tag{2.37}$$

with the number density $\rho_N = \frac{N}{V}$. The interaction of an isolated atom with a light field can be classically described by the displacement $\mathbf{r}$ of the electric charge e from the nucleus which thereby induces the macroscopic polarization $\mathbf{P}$ of the atomic cloud

$$\mathbf{P} = \langle e\mathbf{r} \rangle \cdot \rho_N = \langle \mu \rangle \cdot \rho_N. \tag{2.38}$$

Using equations 2.32 and 2.38 the atomic cross section can be expressed as follows

$$\sigma(\omega) = \frac{1}{\rho_N} \frac{\omega}{c} \cdot \Im \left(\frac{\langle \mu(\omega) \rangle}{E(\omega)} \right). \tag{2.39}$$

Since in typical absorption experiments the intensities $I(\omega, z)$ and I_0 are measured one defines the optical density (OD) as

$$OD(\omega) = \log_{10}\left(\frac{I_0(\omega)}{I(\omega)}\right) = \frac{\sigma(\omega)}{\ln 10} \cdot \rho_N l, \tag{2.40}$$

(with l being the sample thickness) to evaluate the recorded spectra.

For the non-linear case the linear relation in equation 2.32 changes to

$$\mathbf{P}(t) = \epsilon_0 \sum_n \chi^{(n)} \mathbf{E}^n = \epsilon_0[\chi^{(1)}\mathbf{E}(t) + \chi^{(2)}\mathbf{E}^2(t) + \chi^{(3)}\mathbf{E}^3(t) + ...], \tag{2.41}$$

with $\chi^{(n)}$ being a tensor of higher order. The nonlinear polarization components lead to nonlinear terms in the wave equation

$$\Delta\mathbf{E} - \frac{1}{c^2}\frac{\partial^2\mathbf{E}}{\partial t^2} = \frac{1}{\epsilon_0 c^2}\frac{\partial^2\mathbf{P}}{\partial t^2}, \tag{2.42}$$

and thus to generation of new frequency components in the signal. The first term in equation 2.41 referes to the upper explained effect of linear absorption. The second order term describes three-wave mixing processes as for example the famous Pockels effect. Since in this work only the noble gas neon is investigated and gases are inversion symmetric, even-order nonlinearities are suppressed due to symmetry reasons. As the absolute value of $\chi^{(n)}$ decreases with the order n, only third order non-linear effects will be treated in this work. Specially this work will focus on the process of four-wave mixing (FWM).

One can describe four-wave mixing as a superposition of three waves with different frequencies ω_i. The process can be simplified as the first wave with frequency ω_1 generates a polarization in the sample, while the second wave ω_2 interferes with the first thereby generating a grating with components at the sum $\omega_1 + \omega_2$ and difference $\omega_1 - \omega_2$ frequencies. The third and last wave ω_3 then interferes with the original frequencies as well as their sum and differences generating the fourth field ω_4. In the case of the experiments carried out in the laboratory in Heidelberg the incident light fields will have different frequencies ω_i as well as different directions $\mathbf{k_i}$, while for the experiment carried out at the FLASH facility the incident light fields will have the same frequencies ω_i but different directions $\mathbf{k_i}$.

In order to determine the dynamical evolution of the target system the aforementioned laser fields with frequencies ω_i are replaced by ultra short laser pulses

whose bandwidths cover all the considered frequencies ω_i due to the time bandwidth product $\sigma_t^2\sigma_\omega^2 \geq \frac{1}{4}$. The target system is illuminated using these ultrashort laser pulses. Signal spectra are then recorded as a function of the time delays between individual pulses. The time delay $\tau = t_1 - t_2$ between the two pump pulses 1 and 2 is called the coherence time and the time delay $T = t_2 - t_3$ between pulse 2 and the probe pulse 3 is called the detection time. The collected data is presented in the spectral domain by taking the Fourier transform along one of the mentioned time-delay axes as one of the axis is already converted to the spectral domain by the used frequency-dispersive spectrometer. To retrieve the phase of the measured third order response it is common to interfere the signal with a fully characterized weak reference pulse which is called the local oscillator (LO) for heterodyne detection. The FWM sceme for this case can be seen in figure 2.6.

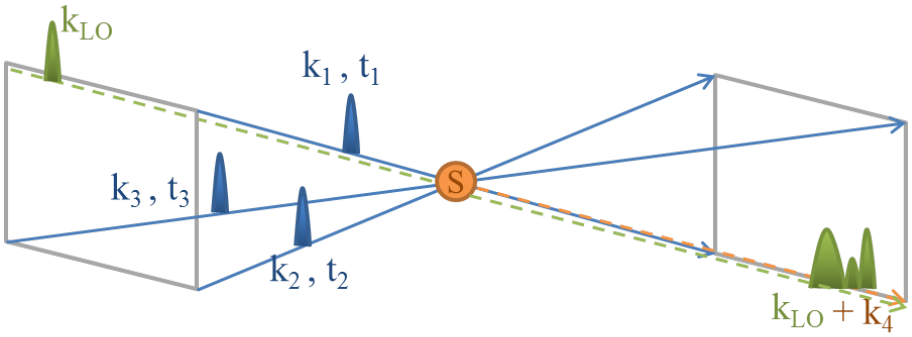

Figure 2.6.: FWM sceme with local oscillator fulfilling boxcars phase-matching geometry. To fully characterize the measured signal a local oscillator (green) is used for heterodyne detection. It is choosen to be collinear with the signal (orange arrow).

Since the in the following presented measurements in neon are first proof-of-principle measurements no local oscillator was used for heterodyne detection. With this in mind the LO will be neglected in the following. When the incoming fields are weak the signal can be treated in the framework of perturbation theory and the third-order polarization in the time domain is given by [22]

$$\begin{aligned} P^{(3)}(x,t) = \int dt_3 \int dt_2 \int dt_1 S^{(3)}(t_3,t_2,t_1) \\ \times E_3(x,t-t_3)E_2(x,t-t_3-t_2)E_1(x,t-t_3-t_2-t_1), \end{aligned} \tag{2.43}$$

with

$$E_1(x,t) = \mathcal{E}_i[e^{i\omega_c t - i\mathbf{k_i}\cdot x} + e^{-i\omega_c t + i\mathbf{k_i}\cdot x}], \tag{2.44}$$

being the electric fields with amplitudes $\mathcal{E}_i$, central frequency ω_c and wave vectors $\mathbf{k_i}$. The term $S^{(3)}(t_3, t_2, t_1)$ is known as the non-linear third-order response of the sample which describes all quantum mechanical interaction pathways the system can undergo during the interaction times t_1 to t_3 and during its free evolution. The temporal phases $\pm i\omega_c$ induce the resonant transitions in the target, while the spatial phase $\pm i\mathbf{k_i}x$ determines the phase difference between the transitions across the interaction volume. A non-collinear (boxcars) geometry which was used in the experiments is shown in figure 2.7. This geometry gives rise to a variety of phase gratings which interfere with each other and give rise to a set of four-wave mixing signals with spatial frequencies for all permutations of $\pm\mathbf{k_1} \pm \mathbf{k_2} \pm \mathbf{k_3}$, radiated into the corresponding spatial direction.

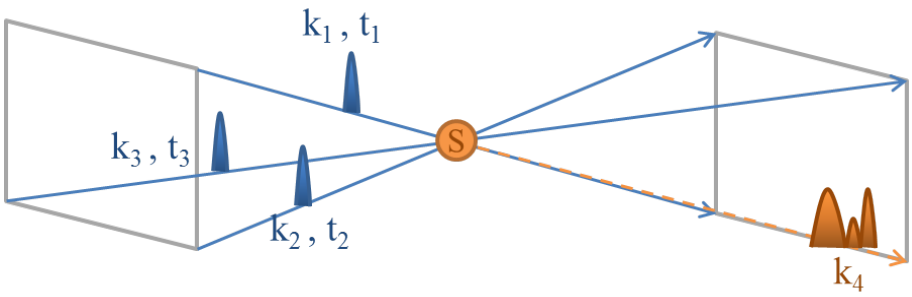

Figure 2.7.: FWM scheme with boxcars phase-matching geometry. The incident beams with wave vectors k_i and temporal distance t_i to the sample (S) are indicated in blue. The wave mixing process which take place in the sample (S) can be understood as transient phase gratings of excitations in the medium induced by the first two incoming pulses (pump pulses). The probe pulse is then diffracted on this transient phase grating and generates the signal which is emitted in direction k_4 (orange arrow).

By setting the wave vectors (due to selecting the specific angles between the three pulses) it is possible to select a specific wave-mixing signal. For the above mentioned boxcars geometry phase matching and energy conservation define a signal in the $\mathbf{k_4}$ direction

$$\mathbf{k_4} = +\mathbf{k_1} - \mathbf{k_2} + \mathbf{k_3}, \tag{2.45}$$

with frequency

$$\omega_4 = \omega_1 - \omega_2 + \omega_3. \tag{2.46}$$

Since the generated four-wave mixing signal is emitted in a different direction as the incident fields it is possible to measure the signal background free.

2.2.4. High-harmonic generation

The XUV light used to carry out the experiments described in this work was generated using high-harmonic generation (HHG). The process of high-harmonic generation is a highly nonlinear frequency conversion process which becomes apparent when the electic field strength approaches the binding energy of the inner-atomic potentials. An intuitive understanding of the process under strong laser fields is shown by the semi-classical three-step model [23] in figure 2.8. It is assumed that the strong linearly polarized electric field bends the atomic Coulomb potential along the polarization axis. If the effective generated energy barrier is narrow enough the electronic wavefunction can tunnel through (step 1). The wave packet is now accelerated by the laser field and gains kinetic energy E_{kin} (step 2). As the field reverses its direction the wave packet is accelerated back to the ion core where it recollides with the ion releasing its excess energy as coherent dipole radiation (step 3).

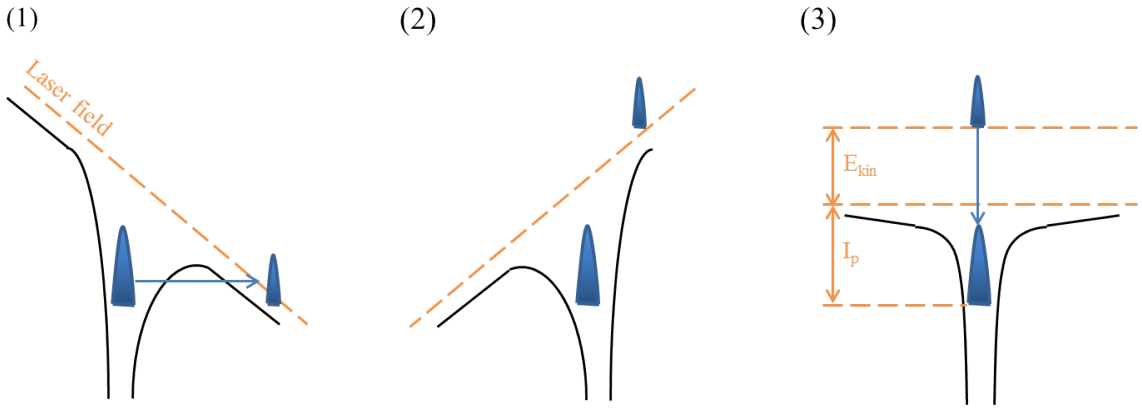

Figure 2.8.: Schematic picture of the three-step model of the high-harmonic generation process with tunneling process (1), acceleration (2) and recombination (3). The black curve represents the effective binding potential in the presence of the laser field (orange) for an electron wavefunction (blue shaded).

Assuming the wave packet recombines back to the ground state, the emitted energy is given by

$$\hbar\omega_{hhg} = I_p + E_{kin}, \tag{2.47}$$

with the ionization potential I_p and kinetic energy E_{kin}.
Since a bunch of different electron recollision trajectories are possible, different kinetic energies and recollision times are possible. Since these interfere with each other the produced HHG radiation is emitted continously over about a half an optical cycle of the fundamental light field. This leads to the fact, that the produced HHG spectrum

covers a broad photon energy spectrum up to the cutoff frequency that corresponds to

$$\hbar\omega_{cutoff} = I_p + 3.17U_p, \tag{2.48}$$

with the ponderomotive potential $U_p = (e\mathcal{E}_0)^2/4m_e\omega_{laser}^2$. The poderomotive potential describes the average quivering energy of a free electron in an oscillating laser field with the electron charge e, the field strength $\mathcal{E}_0$, the electron mass m_e and the laser frequency ω_{laser}.
The HHG process is periodically repeated each laser half cycle therefore all generated XUV fields interfere giving rise to a $2\omega_{laser}$-spaced frequency comb in the spectral domain. Due to the inversion symmetry of the recollision process (step 3) in the gas medium the HHG spectrum only consists of odd harmonic components. An in neon created HHG spectrum can be seen in figure 2.9.

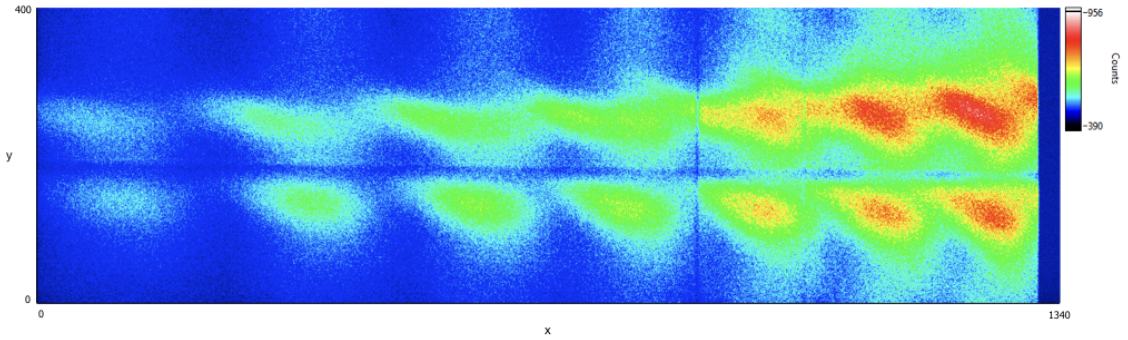

Figure 2.9.: Measured full-chip image of in neon generated high harmonic light. For this picture the generated HHG light was afterwads focussed into the target cell filled with neon. Due to the absorption of the target two absorptionlines appear in the HHG spectrum. The axes x and y are the respective full-chip axes and the colorbar represents the amount of counts for each pixel.

2.2.5. Free-electron laser

Nowadays free-electron lasers (FELs) provide laser radiation ranging from microwaves up to X-ray. Therefore each FEL is specified at a specific wavelength range. The lasing medium consists of high-speed electrons moving freely through a magnetic structure, hence the name free-electron laser. Free-electron lasers consists in principle of three main parts: the photoinjector, the accelerator and the undulator. In the following the FEL at the FLASH facility in Hamburg will be explained in detail since this was the FEL which was used for the all-XUV four-wave mixing experiments.

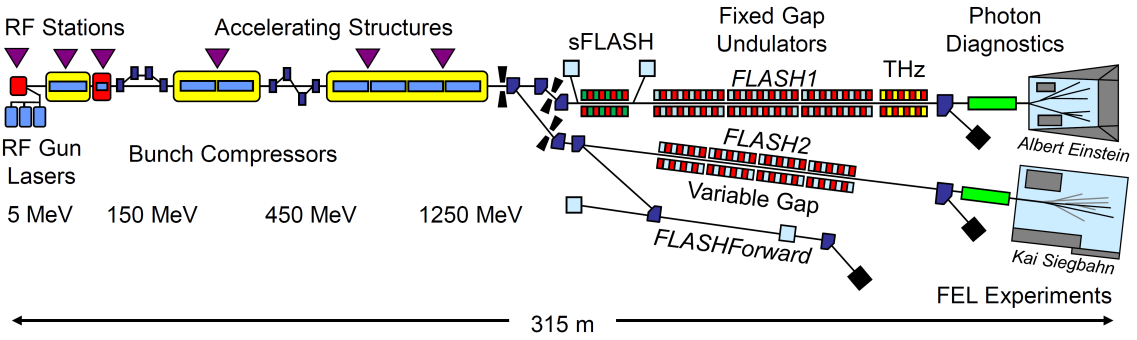

Figure 2.10.: Schematic drawing of the FLASH facility. The experiments were carried out at FLASH1. The FEL aparatus used has therefore no variable gap undulators. See the main text for further description. This figure is reprinted from [24].

In the first step a bunch of free electrons is generated in the photoinjector which is in this case based on a laser-driven radio frequency (RF) photocathode electron gun. The produced photoelectrons from the photocathode are then accelerated by the superconducting linear accelerator up to highly relativistic speeds on the order of GeV. In order to reach high charge densities in the undulator the beam is compressed along its axes by bunch compressors. After passing the accelerating structures and the bunch compressors the beam is deflected into the soft X-ray undulators where the process of coherent light generation takes place. The undulator consists of a set of two planes of permanent magnets with peak strenghts up to 0.47 T. The permanent magnets are arranged in an alterning manner with a fixed gap of 12 mm between the planes and a periodicity of 27 mm. The electrons which travel now along the z-direction through the undulator experience the periodic magnetic field in the vertical y-direction and start therefore to undergo a wiggle motion in the horizontal x-direction.

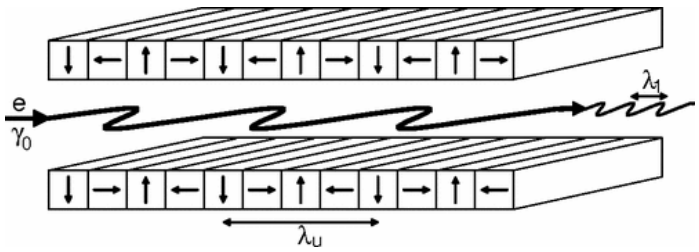

Figure 2.11.: Schematic drawing of one undulator. The in z-direction travelling electrons experience the periodic magnetic field in the y-direction and therefore undergo a wiggle motion in the horizontal x-direction, thereby emitting synchroton radiation. This figure is reprinted from [25].

This motion leads to the emission of synchrotron radiation as expected for an accelerated charge. The magnetic field

$$B_y = B_0 \cdot sin\left(\frac{2\pi}{\lambda_u} z\right), \tag{2.49}$$

with field strength B_0 and undulator period λ_u gives rise to the emitted radiation with wavelengh

$$\lambda_r = \frac{\lambda_u}{2\gamma_0^2}\left(1 + \frac{K_0^2}{2} + \gamma_0^2\phi^2\right), \tag{2.50}$$

with the energy of the electrons γ_0 in units of the rest-mass energy $m_e c^2$, the undulator strength parameter $K_0 \propto B_0\lambda_u$ and the radiation angle ϕ in terms of the undulator axis. Since only the radiation emitted along the propagation axis is of interest, ϕ is set to zero and the resonant wavelength in forward direction is given by

$$\lambda_1 = \frac{\lambda_u}{2\gamma_0^2}\left(1 + \frac{K_0^2}{2}\right). \tag{2.51}$$

During one undulator period the radiation overtakes the electrons by λ_1.

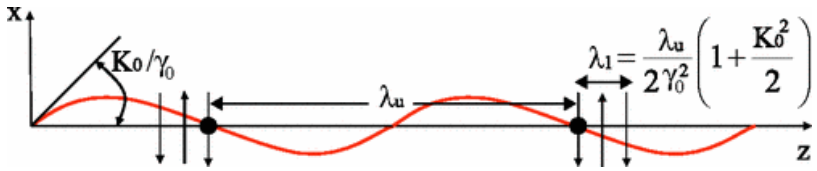

Figure 2.12.: This figure shows how the micro-bunching effect is created. While the electron (depicted as black dot) travels the distance λ_u of the sinusoidal trajectory (depicted in red), the generated radiation (alterning vertical errors) is faster by one resonant wavelength λ_1. The energy exchange between the electrons and the generated radiation leads to micro-bunching. This figure is reprinted from [25].

Depending on the relative phase between the plane wave and the electrons, some of them will gain energy while other release energy to the electromagnetic field. This results in a periodic modulated energy density within the electron bunch. This energy modulation evolves into a charge density modulation and is called micro-bunching. The micro-bunch spacing corresponds to the scale of the resonant wavelength λ_1. By fulfilling the resonance condition the micro-bunches generate coherent light. This process of self-amplified spontaneous emission (SASE) allows for exponential gain of the spontaneous emission.

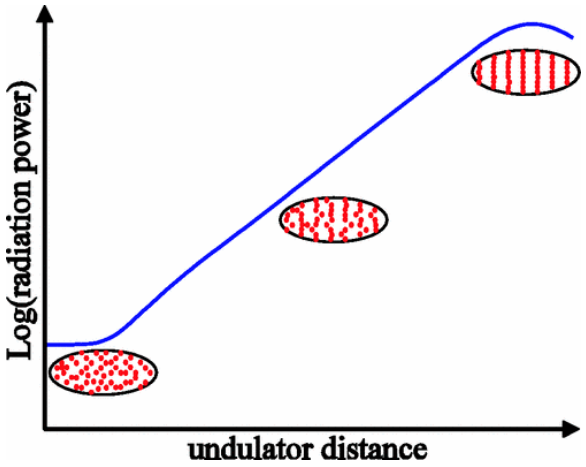

Figure 2.13.: The process of self-amplified spontaneous emission (SASE) leads to an exponential gain of the spontaneous emission. This figure is reprinted from [25].

3. Stability and temporal overlap

3.1. Interferometric setup for stability measurements

To measure the stability of the X-MuSIC (X-ray/XUV Multidimensional Spectroscopy and Impulsive Control) beamline a HeNe laser (red arrow in the sceme) was directed into the beamline (which will be explained in detail in Chapter 4). There it passes first the toroidal mirror (T) which generates the focus of the beam 70cm downstream. After a distance of 70cm past the torodal mirror the CMOS camera (C) is placed on a micrometer stage to fine tune the distance and to allow the camera to be in the focal spot of the focussed beam. After the toroidal mirror the HeNe laser passes the mirror unit (S) consisting of the split-mirror (with mirrors 1-4) and the hexapod positioner. The hexapod positioner is therefore used to place the split-mirror the way that only two respective mirrors were illuminated (e.g 1 and 2 as depicted in the scheme). Thus the HeNe laser beam will be split into two identical beams. For the stability measurements one mirror is kept at a fixed position while the second one is delayed with respect to the first. After the split-mirror a simple silver-coated reflective mirror (M) is placed into the beams to couple the light through a laser grade window out of the vacuum chamber. After the laser grade window the HeNe laser propagates through air until it hits the CMOS camera. The used HeNe laser is fixed placed on the laser table and is normally used to prealigne the optics on the laser table where the Ti:Sa laser later on passes through for experimental purposes. Since this adjustment HeNe laser passes through the same optics as later on the Ti:Sa laser it can be assumed that the measured stability which will be a sum of vibrations of turbo pumps and vibrations of used optics describes the experimental circumstances best.

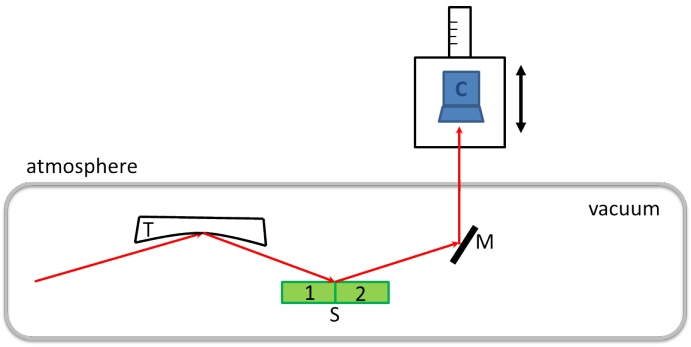

Figure 3.1.: Setup sceme for stability measurements, T is the toroidal mirror, S the split-mirror unit, M the silver-coated reflective mirror and C the CMOS camera.

3.2. Data evaluation and results

It has to be noted that all stability measurements were carried out under experimental conditions so that the true stability during an actual experiment is measured directly. For this purpose the turbo pumps were turned on as so were the other motorized stages as for example the tip-tilt stages and the hexapod on which the 4-split-mirror was mounted. The entire setup can be seen in figure 4.1. For all stability measurements the delay stage of one mirror is kept fixed while the other is scanned with a stepsize of 0.05 μm. One measured intensity trace can be seen in figure 3.2(a). As can be seen the intensity trace consists of an intensity offset and the sine modulation which is produced due to the interference of the two beams. Since we were only interested in the deviations from a perfect sine oscillation the data ist Fourier transformed so that one can separate the different frequency parts. In figure 3.2(b) one can clearly see the DC-peak from the envelope at around 0 $\frac{1}{\mu m}$ and the contibution of the fast sine oscilation at about 28 $\frac{1}{\mu m}$. To get rid of the DC-peak the supergauss filter

$$f(x) = e^{-((x-\mu)/\omega)^n}, \tag{3.1}$$

with mean μ, width ω and power n is used. The supergauss filter which was used for the further evaluation is shown in 3.2(c) and had the parameters: $\mu = 0\frac{1}{\mu m}$, $\omega = 20\frac{1}{\mu m}$ and $n = 8$. The filtered Fourier spectrum is shown in figure 3.2(d). Since we are interested in the fluctuations of the system the data is Fourier transformed back and the argument is extracted which represents the phase of the measured signal. In the next step a linear function is fitted to the data and the difference between linear fit und phase is determined in units of time. To convert from phase to time the difference values are multiplied by the factor $\lambda_{hene}/c \cdot 2\pi$.

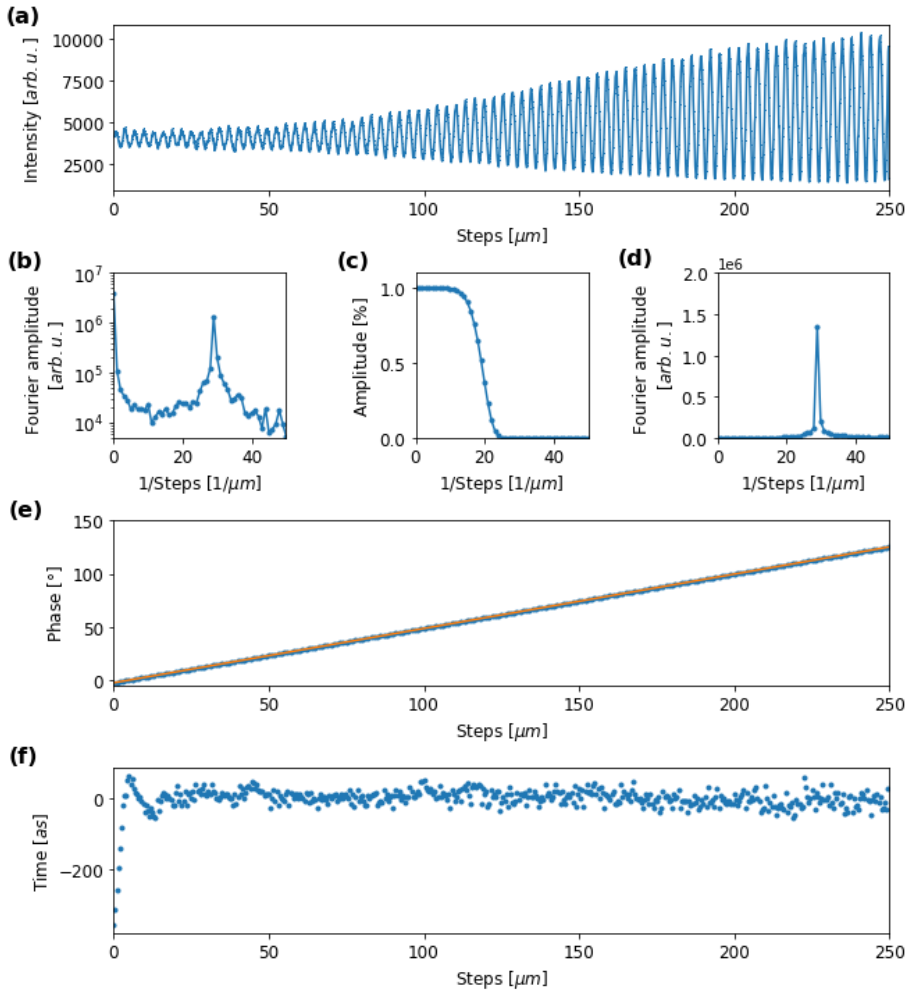

Figure 3.2.: Evaluation scheme, (a) shows the interferometric measured intensity fringes as function of the driven steps, (b) shows the corresponding Fourier plot of (a), (c) shows an example of the used supergaussian filter to filter out the DC peak, (d) is the result of (b) after applying the filter shown in (c). (e) shows the extracted phase and fit to the phase. (f) shows the difference between the data and the fit in units of time. The artefact from the Fourier filtering method which can be clearly seen for the steps 0 to 10 was excluded since it is no real measured effect.

Since the four-quadrant mirror first only consisted of two mirrors for transient absorption measurements and was updated to four mirrors the stability of both configurations was measured to determine wether the change in the system influences its stability. For this purpose the data was taken for the two- (blue) as well as for the four-mirror configuration (orange). Since the system should be stable over the full delay range the full data is binned to a histogram. As can be seen in figure 3.3 there is a huge difference in the spread of the deviation if the hexapod is turned on. There

is also a change between the two- and the four-mirror configuration which will be investigated later.

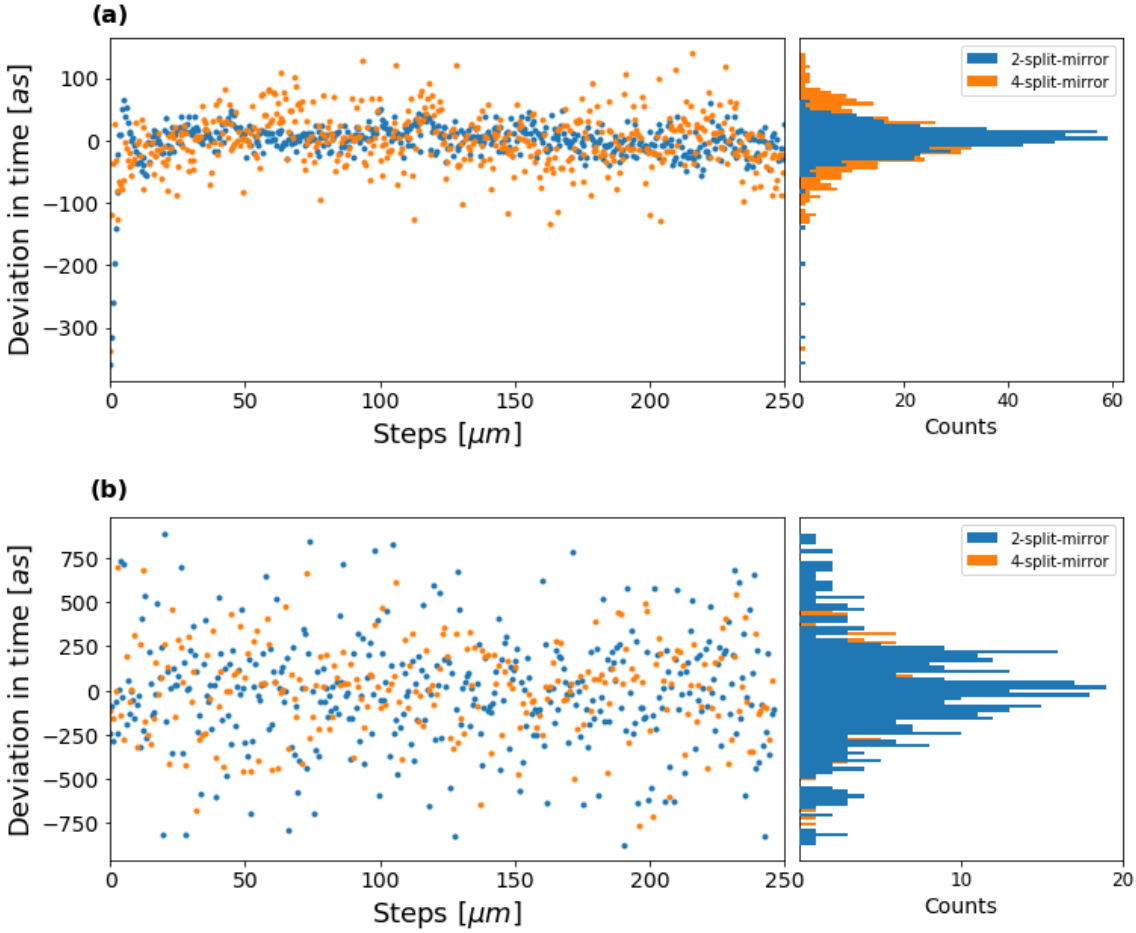

Figure 3.3.: Comparison of the stability between the 2- an 4-split configuration, on the lefthand side the deviations are plotted as a function of the steps driven. Blue denote the 2-split configuration and orange the 4-split configuration. (a) shows a measurement where the hexapod was turned off and (b) shows an analog measurement where the hexapod was turned on. As can be easily seen the stability is way better for the case when the hexapod was turned off independent of the chosen mirror configuration.

To quantify the temporal stability of the split-mirror the four histograms from figure 3.3 are fitted to a gaussian error distribution according to

$$f(x) = a \cdot e^{-(x-x_0)^2/2\sigma^2}, \tag{3.2}$$

with the amplitude a, mean x_0 and standard deviation σ which corresponds to the stability. The fit results are shown in figure 3.4 and 3.5.

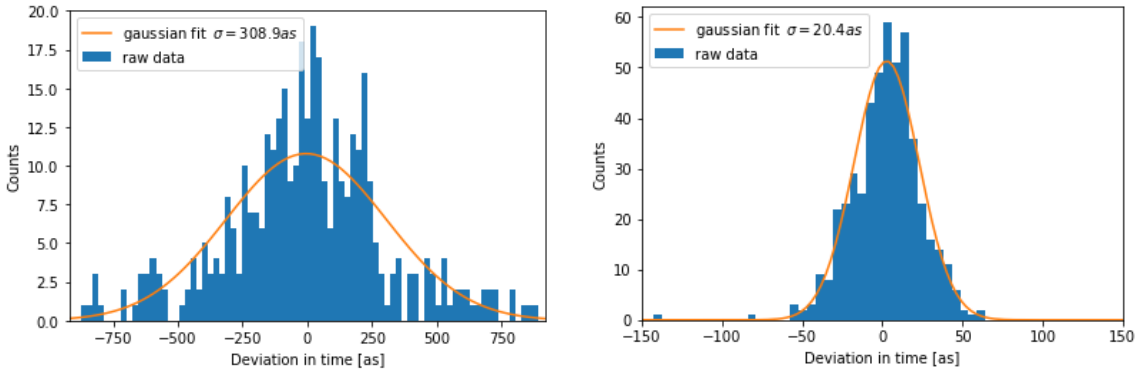

Figure 3.4.: Histograms for the 2-split-mirror configuration. The raw data is shown in blue, while the fits are shown in orange. On the left the result for the hexapod on case, resulting in a stability of 308.9 as. On the right-hand side the same measurement with the hexapod turned off. The fit determines the stability with 20.4 as.

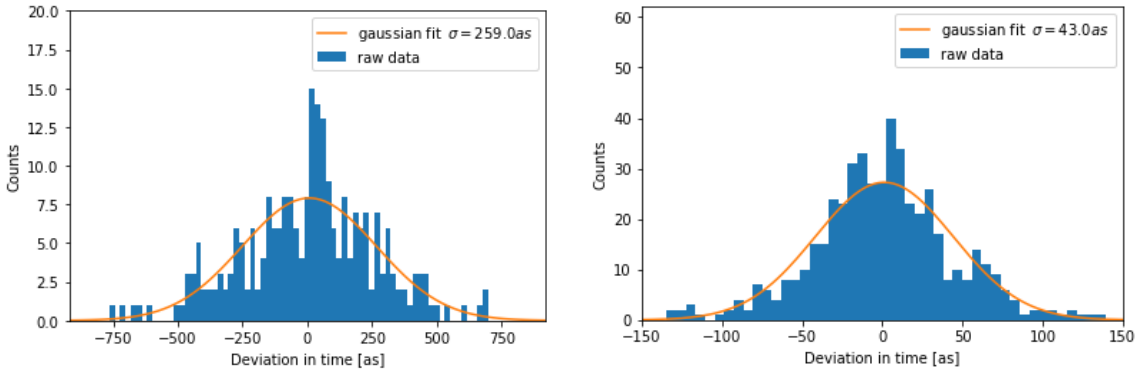

Figure 3.5.: Histograms for the 4-split-mirror configuration. The raw data is depicted in blue, while the fits are shown in orange. On the left the result for the hexapod on case, resulting in a stability of 259.0 as. On the right-hand side the same measurement with the hexapod turned off. The fit determines the stability with 43.0 as.

One has to note that for the gaussian fit the artefact from the Fourier filtering method which can be clearly seen in figure 3.2(a) for the steps 0 to 10 was excluded since it is no real measured effect. As can be seen the measured data is well described by the gaussian error distribution since the fluctuations seem to be randomly distributed. The conclusion of this result leads to the insight that for experiments the hexapod should be turned off so that it cannot influence the experiments. This huge effect on using the hexapod was not expected since the hexapod should move the mirrors by the same amount so that no relative movement between the mirrors is induced. However movements of the hexapod positioner seem to influence the feed-back loops of the individual delay stages. They start so oscillate around their

target position which leads to position instabilities in time. Turning off the hexapod improves the stability of the system by a factor of 10 which can be crucial in time delay measurements with sub-femtosecond time resolution.
There is still the open question why the stability between the 2-split and 4-split-mirror setup differ by a factor of 2 in magnitude. Possible reasons for a worse stability could be the split-mirror itself or fluctuations which arise from the HeNe laser. This could be fluctuations in its intensity or in frequency. Normally a laser can be intensity- or frequency-stabilized, both is not possible. Frequency instabilities can be crucial since they change the spacing between the interference fringes and can not be filtered out easily. To find out whether the instabilities arise from intensity or other fluctuations, the normalized data was determined. In this case the intensity trace which was measured for a small part of the interference pattern (see white rectangle in figure 3.6) was normalized to the total measured intensity of the camera chip.

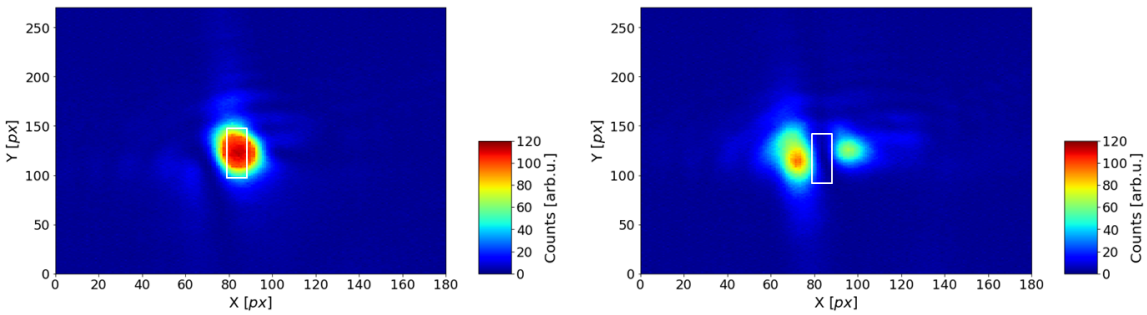

Figure 3.6.: Two exemplary full-chip images of the measured intensity fringes on the CMOS camera for different mirror positions. The non-normailzed histograms were evaluated by counting the amount of counts in the yellow rectangle in figure 3.6. Since the interference pattern changes the measured signal in 3.2(a) has a sinusoidal course. For the normailzed histograms the intensity fluctuations of the complete CMOS chip were measured and 3.2(a) divided by it. The normalization can only compensate for intensity fluctuation. Phase fluctuations which change the frequency of the measured sinusoidal pattern can not be compensated by this technique.

With this method it is possible to extract intensity instabilities of the HeNe laser. Pointing and frequency instabilities cannot be factored out by this technique. As can be seen it is only possible to improve the stability by about 10 percent. Intensity fluctuations are therefore not the reason for the big difference in stability between the two- and the four-mirror configuration. To determine the stability of the mirrors a

frequency-stabilized laser should be used so that one can assume the fringe spacing to be constant and could calculate the instabilities of the intensity by normalizing. This way it is not possible to determine whether the worse stability comes from the mirror itself or the laser. The measurement was repeated at another experimental setup which resulted in the same degraded stability. With this in mind it seems clear that the HeNe laser has degraded over time and that it is not possible to compare the stability of the 2- and the 4-split configuration directly.

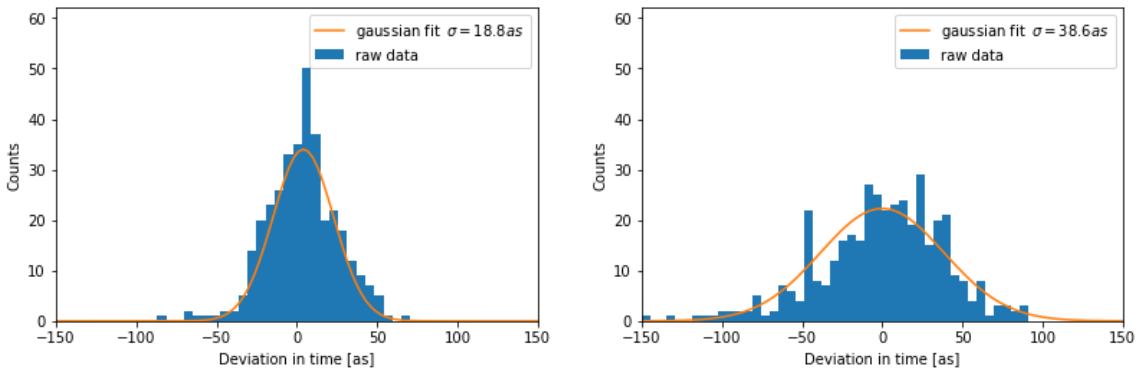

Figure 3.7.: Histograms and fits for the normalized stability measurements. On the left the stability of the 2-split and on the right for the 4-split configuration. As can be seen the stability can only be improved by about 10 percent.

3.3. Determining temporal overlap

In this chapter the temporal overlap between the individual mirrors is determined. For this a Ti:Sa laser was used since it has a far smaller pulse/coherence length than the previously used HeNe laser. For this part only two mirror segments were illuminated. One was kept at the fixed position of 0 μm while the second was scanned in 0.05 μm steps. The intensity was again measured in the focus of the two spatially overlapping beams with a CMOS camera. The measured signals for the respective mirrors can be seen on the top graph of figure 3.8 (a) and (b). In which (a) shows the data for the temporal overlap between mirror 2 and 3 and (b) shows the data for the mirrors 2 and 4. Since for the determination of the temporal overlap only the central position of the measured oscillation is needed, the fast oscillations are filtered out by Fourier filtering. The absolute intensity after filtering is plotted on the bottom graph of 3.8 (a) and (b). The central peak positon was determined and

fitted to the absolute intensity with a combination of a linear and gaussian function corresponding to

$$f(x) = b + c \cdot x + a \cdot e^{-(x-x_0)^2/2\sigma^2}, \tag{3.3}$$

with fit parameters a, b, c, overlap position x_0 and standard deviation σ.

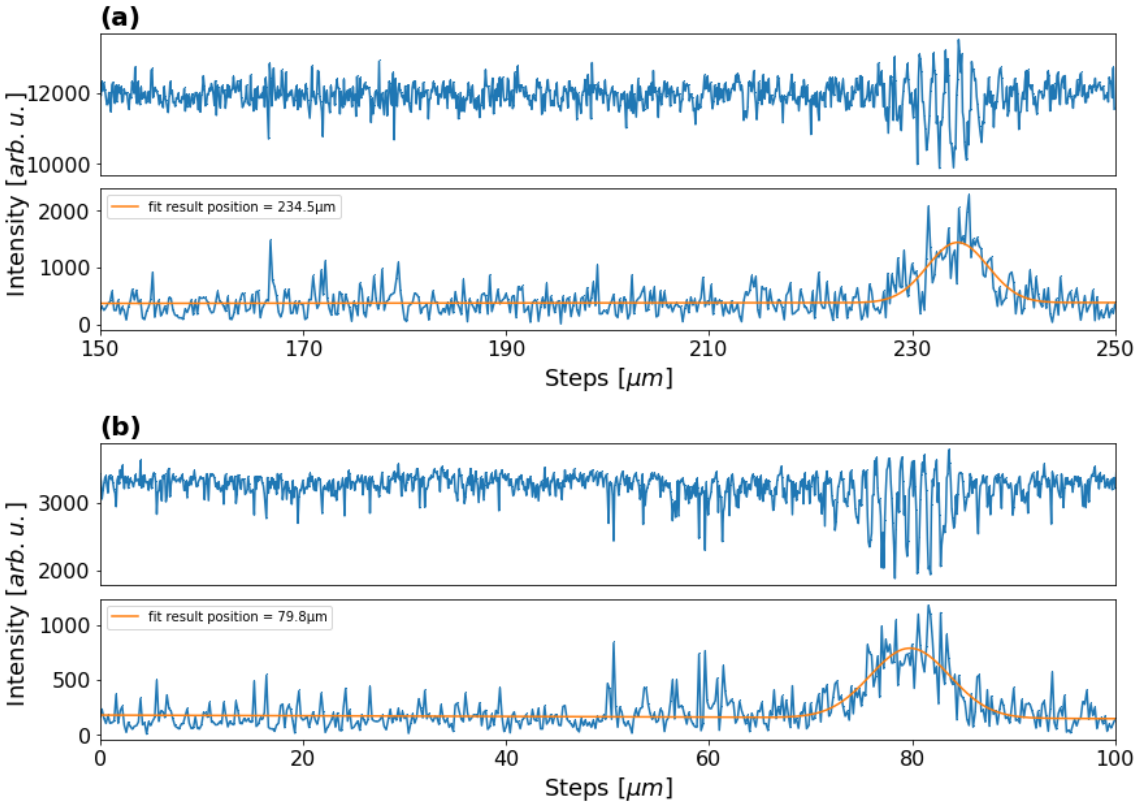

Figure 3.8.: Interferometric determination of the temporal overlap between the individual mirrors with a Ti:Sa laser. The upper graphs show the measured intensity fringes and the lower graphs show the corresponding intensity envelopes. The raw data is shown in blue and the fit result in plotted in orange. (a) shows the data of the measurement for the temporal overlap between the mirror 2 and 3. The fit results in optimal temporal overlap at 234.5 μm. In part (b) the temporal overlap between 2 and 4 investigated. It turns out that temporal overlap is at 79.8 μm.

The temporal overlap positions which were estimated by the fit function 3.3 can be read out from figure 3.8 and are summarized in table 3.1. The temporal overlap between the mirrors 2 to 4 and the local oscillator (1) could not be determined. This

could be since the LO is out of the reach of the time delay stage or the reflectivity of the local oscillator is too little in comparison to the other mirrors. This could be possible since for the local oscillator not a simple mirror but a reflective grating was built in. To get the overlap position in units of time the following geometrical formula is used:

$$x[fs] = \frac{x[m]}{c} = 2d \cdot \sin(\alpha). \tag{3.4}$$

Plugging in the grazing incidence angle of 15 degree and the step d as 1 μm gives a conversion factor relation of:

$$1\mu m = 1.727 fs. \tag{3.5}$$

Mirror	Position [μm]	Position in time [fs]
2	0	0
3	234.5	405.0
4	79.8	137.8

Table 3.1.: Summary of temporal overlap positions for the three used mirrors. To convert from μm to fs delay the factor relation 3.5 was used.

4. NIR-NIR-XUV four-wave mixing experiments in neon

4.1. Laser system and experimental setup for HHG experiments

For the following experiment a femtosecond laser system (Femtolaser HE/HR) is used. The laser system can be operated in a carrier envelope phase (CEP) stabilized mode, which was not used for this work since the performed experiments are not sensitive to the CEP. The system is based on chirped pulse amplification and a grating compressor and delivers a pulse energy of 3 mJ at a 3 kH repetition rate with sub-20 fs pulse duration. After the laser output the pulses are focussed into a hollow core fiber which is filled with helium gas at a pressure of 2 bar. Self-phase modulation within the fiber leads to a spectrally wider pulse afterwards with the spectral components dispersed. To compress the now spectrally broad pulses in time a chirped mirror compressor is used. It consists of multi-layer reflective mirrors for which light at different wavelengths is reflected at a different penetrating depth. Therefore the red components of the pulse will propagate deeper into the mirror in comparision to blue components which are reflected at the first layers. Since the red components propagate deeper it is possible to compensate the dispersion and therefore to shorten the pulse in time. After the chirped mirrors the pulses have a temporal duration of sub-5 fs and still a pulse energy of 1 mJ.

These pulses are afterwards focused into the HHG-cell. The HHG-cell is a vertical tube of stainless steal with two 200 μm holes on opposite sites for the laser to pass through. Due to the the small focal spot the beam reaches peak intensities of about $1{\cdot}10^{15}$ Watt/cm^2 which allows the process of high harmonic generation to be driven effectively. To optimize the XUV flux 200 mbar of neon gas were applied. The HHG-cell can be moved along all three dimensions to optimise high-harmonic

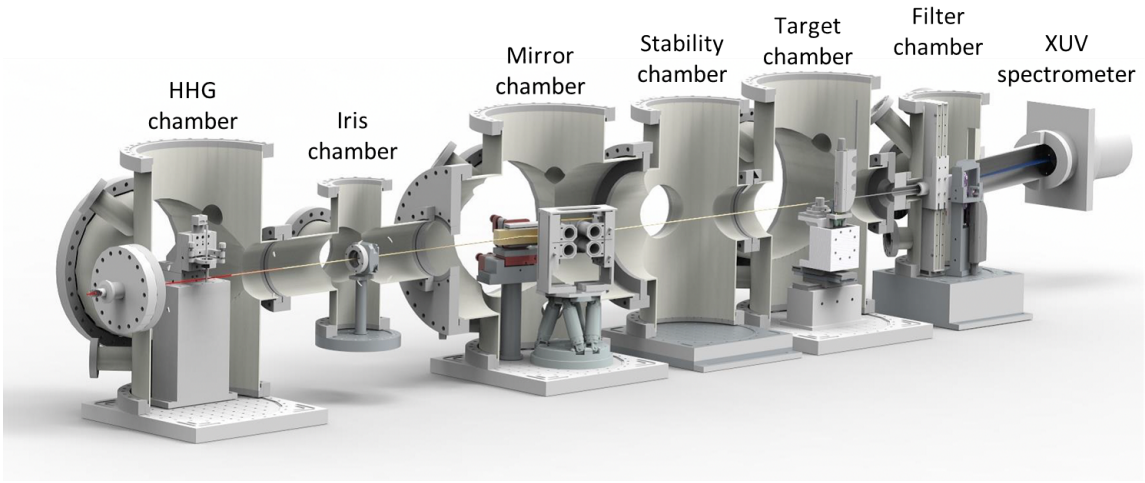

Figure 4.1.: Sketch of the X-MuSIC beamline. The laser pulse (red line) is focused into the beamline through the entrance window on the left-hand side of the HHG chamber. There it passes the gas-filled HHG-cell where due to HHG attosencond XUV pulses (yellow line) are generated. Now NIR and XUV copropagate through the beamline. The NIR intensity can be reduced by the motorized iris in the iris chamber. The mirror chamber contains the toroidal mirror which can be seen from the front and the four-quadrant split-mirror which can only be seen from the back in this image. After splitting the light into four parts the light passes the stability chamber (where the mirror for outcoupling is faded out in this sketch) and hits the target cell. Afterwards the NIR is filtered out by the filter unit in the corresponding chamber and the remaining XUV light and signal pass the spectrometer (blue line) and are measured on the XUV detector.

generation via phase-matching. After this process both the NIR and the XUV light (denoted in figure 4.1 in yellow) copropagate. Since the XUV light has a smaller divergence it is mainly positioned in the middle of the two copropagating beams while the NIR is located over the entire beam profile. By a motorized iris aperture it is possible to control the intensity of the remaining NIR light without desturbing the XUV. This can be seen in the second vacuum chamber. The following chamber contains the important optics and is therefore in the following called the mirror chamber. It contains the toroidal mirror as refocussing optic and the four-quadrant split-mirror as split-and-delay unit. For optimized reflection in the XUV and NIR spectral region gold coated optics under an grazing incidence angle of 15 degrees are used. The toroidal mirror images the focal spot in the HHG-cell into the target with a 2f-2f geometry, providing an imaging ratio of 1:1. The focal lengh of the toroidal mirror is given as f = 350 mm, so that the distance between the toroidal mirror and both foci correspond to 700 mm. After the refocussing optic both the XUV and NIR light hits the four-quadrant split-mirror and is split into four identical parts. In order

to minimize losses due to the gap between the mirrors, they are mounted as close as possible. How big the gap between the respective mirrors is was not directly measured in this work. One of the mirrors is mounted fix and has the purpose to act as the local oscillator (LO). Since it was not used in the experiments described in this work, it will be neglected in the following. Except for the LO the other three mirrors were mounted on delay stages which provide a range of 250 μm with a nominal precision of 1 nm. Under the grazing angle of 15 degree the driving range of the delay stages translates into a total delay of 430 fs. As shown in the previous chapter the stability of the individual mirrors decreases due to vibrations induced by the surrounding experimental parts like the turbo pumps or for example the hexapod positioner. Additionally to the delay stages each mirror is also mounted on a tip and tilt stage which is depicted as the cylindrical part in Figure 4.2. The tip-tilt stages provide an individual tilting ability of 5 mrad with a precision of 0.05 μrad and are crucially needed to achieve beam overlap in the target for different delay positions. In order to account for different experimental conditions or to run different kinds of experiments without bigger efforts, the four-quadrant split-mirror is mounted on a hexapod positioner, which is a high precision stage with 6 degrees of freedom. It enables to react to changes in beam pointing as well as changing the number of mirrors illuminated. Also the intensity ratio between the individual mirrors can be adjusted by moving the entire mirror setup with respect to the beam axis.

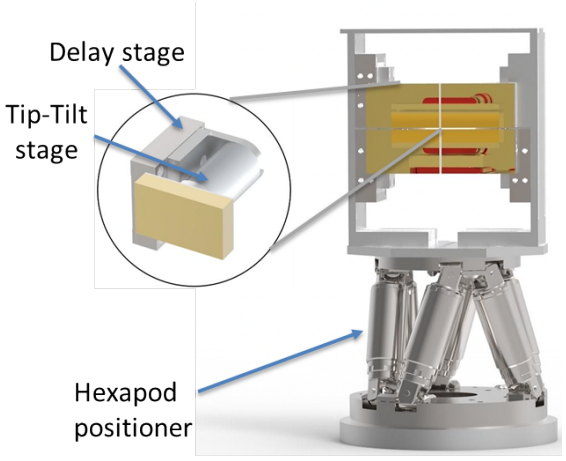

Figure 4.2.: Four-quadrant split-mirror mounted on a hexapod positioner. On the left a detailed view of one split mirror with implemented delay and tip-tilt stages is presented.

The next vacuum chamber contains the outcoupling mirror which was used for the previous stability measurements. Since it is not used for the experiment it is not

depicted in Figure 4.1. The next chamber after this contains the target cell which itself is equal to the HHG-cell. The target cell is also mounted on a 3-axis translation stage to optimize the measured signal in the focus. For the experiments a pressure of 50 mbar of neon gas where applied in the target cell. The final chamber represents the spectrometer which consists of a filter unit, a variable line spacing grating (VLS) and the XUV detector. To prevent leakage through the used aluminium filters and stray light from the previous chambers the filters were stacked in numbers of two to guarantee completely blocking the NIR light. For the following measurements 400 nm of aluminium filters were used in total. The VLS grating which is positioned in the middle of the camber disperses the different wavelenghts onto the detector. The special quality of the grating is that it refocusses the first order onto a flat field. This enables the detector chip which is placed in this plane to detect all energies over its entire lenght with comparable resolution. The VLS grating is optimized for the energy region between 20 eV and 120 eV, corresponding to 62 nm to 11 nm. The XUV detector is a backside-illuminated XUV-CCD camera which provides 1340x400 pixels with an effective pixel size of 20 μm. Since the camera chip can only observe 27 mm of the 110 mm long flat image plane of the grating it is mounted on a mechanical bearing which allows to position the camera chip on the desired mm range. To reduce electrical noise the chip can be Peltier cooled down to -30 degrees Celsius. This option was used in the following measurements.

4.2. Experimental motivation

The first four-wave mixing experiments in neon in this group have been achieved in earlier works [8] with a collinear setup using high-harmonic generated XUV light as well as NIR laser pulses. This led to first measurements of the coherent inner shell wave packet of excited states of different orbital quantum numbers, l = s, p, d.
In the previous work a perturbative NIR pulse (photon intensity = 1 - 10% of the NIR probe intensity) was locked in temporal overlap with the XUV. This XUV/NIR two-color pulse acts as a pump and creates a coherent superposition of the neon $1s^2 2s 2p^6 3d$, $1s^2 2s 2p^6 3p$ and $1s^2 2s 2p^6 3s$ states. As probe pulse a second NIR pulse is used, which couples again the $1s^2 2s 2p^6 3d$, $1s^2 2s 2p^6 3p$ and $1s^2 2s 2p^6 3s$ states. This coupling leads to constructive or destructive dipole emission of the $1s^2 2s 2p^6 3p$ state, periodic in time delay with the full NIR optical cycle, which can be seen in figure 4.3. A schematic level scheme of the experiment can be seen in figure 4.4.

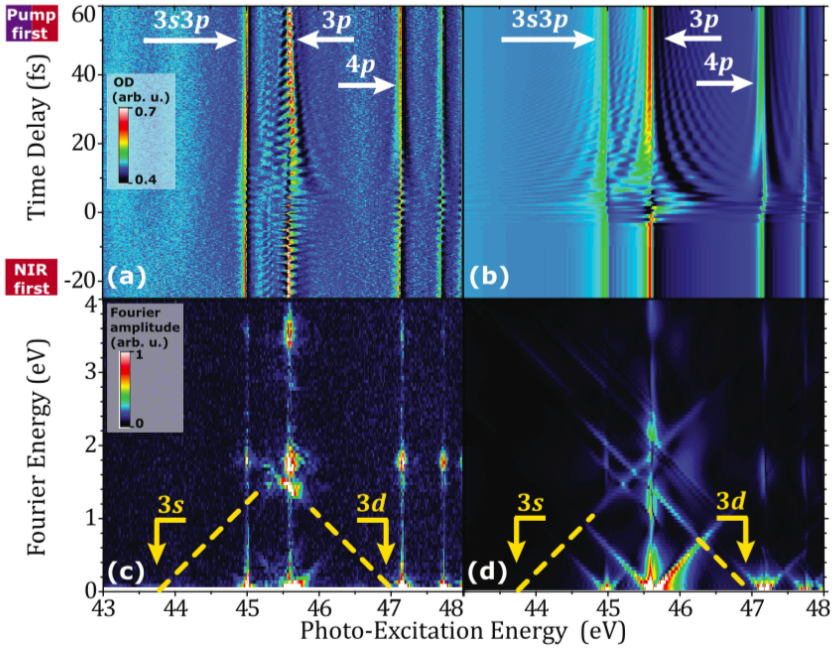

Figure 4.3.: Time-resolved 2D absorption spectra at about 10^{12} W/cm^2 NIR probe intensity obtained from experiment (a) and (b) full ab initio calculations assuming gaussian pulses. Periodic full-cycle modulations are imprinted on the $1s^22s2p^63p$ resonance which give rise to diagonal, line-like peaks at about 1.7 eV Fourier energy (c) and (d), indicating coupling pathways. The energetic position of the dipole-forbidden $1s^22s2p^63s$ and $1s^22s2p^63d$ coupling partners are indicated by the dashed lines. This figure is reprinted from [8].

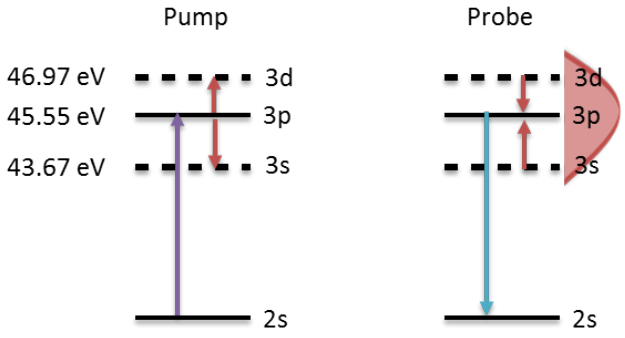

Figure 4.4.: Level sceme for the involved states in neon. In the first step the XUV/NIR pump creates coherent superposition of the states $1s^22s2p^63d$, $1s^22s2p^63p$ and $1s^22s2p^63s$. In the second step the NIR probe (spectrum depicted on the right) couples again the $1s^22s2p^63d$, $1s^22s2p^63p$ and $1s^22s2p^63s$ states. This leads to constructive or destructive dipole emission (blue arrow) of the $1s^22s2p^63p$ state, periodic in time delay with the full NIR optical cycle. The energies of the depicted states are based on [20].

The reason for coupling all three states at once is based on the time-bandwidth

product. A light pulse is in general limited by its time-bandwidth product

$$\Delta t \cdot \Delta \nu \geq C, \tag{4.1}$$

with temporal and spectral widths Δt, $\Delta \nu$. The constant C is dependent on the pulse shape. For a gaussian pulse (which will be assumed in the following) the constant is given by $C = \frac{2 \ln 2}{\pi} \approx 0.44$. Assuming a gaussian femtosecond pulse with a pulse duration of 7.5 fs its bandwidth limit is due to equation (4.1) given by 0.24 eV (FWHM). For a NIR pulse with a cental energy of 1.7 eV it is so possible to interact with states that are separated in energy from 1.35 eV to 2.05 eV. Based on [20] the corresponding state energies are:

$$h\nu_{3p} = 45.55eV, \quad h\nu_{3d} = 46.97eV, \quad h\nu_{3s} = 43.67eV, \tag{4.2}$$

with the Planck constant h.
Therefore states $1s^2 2s 2p^6 3p$ and $1s^2 2s 2p^6 3d$ are separated by 1.42 eV, while the energy separation between states $1s^2 2s 2p^6 3p$ and $1s^2 2s 2p^6 3s$ is given by 1.88 eV. Since the NIR spectrum ranges from 1.35 eV up to 2.05 eV it is therefore possible to couple the $1s^2 2s 2p^6 3p$ state to the both dark states simultaneously.
If it is desired that only one of the couplings is induced one could use a continous-wave (cw) laser with a fixed frequency of 1.42 eV or 1.88 eV depending on which state should be coupled. Another possiblity is to use two NIR femtosecond pulses and to delay these two in time with respect to each other. For this case the spectrum of the resulting double-pulse sequence is modulated in frequency space. Two examples can be seen in figure 4.5 for two NIR pulses with pulse durations of 7.5 fs and central energy 1.7 eV.
Since the $1s^2 2s 2p^6 3d$ and $1s^2 2s 2p^6 3s$ states are not equidistant separated from the $1s^2 2s 2p^6 3p$ state it is possible to generate a frequency modulation for which only one of the two coupling is pronounced. For a schematic example see figure 4.6. Using the two-pulse sequence has the advantage that the time resolution given by the pulse duration can be mantained (which is not the case for a cw laser) and additionally the frequency spectrum can be controlled.
By repeating the experiment from [8] with a frequency-modulated NIR probe it should be therefore possible to specifically address only one of the dark state couplings.

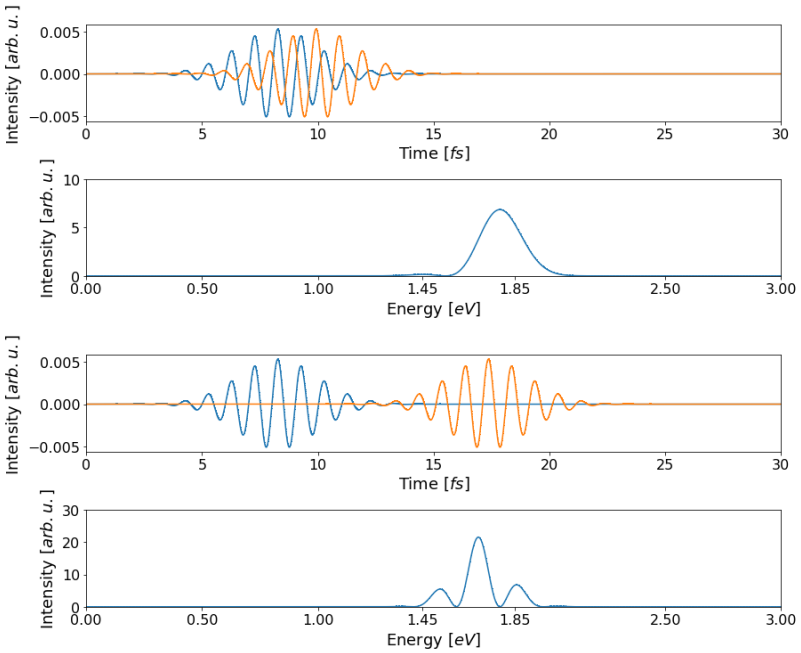

Figure 4.5.: Generated spectral fringes for NIR pulse delays of 4 fs and 22 fs. For this simulation gaussian pulses with a temporal width of 7.5 fs and a central frequency of 1.7 eV were chosen. As can be seen for both cases it is possible to generate a frequency pattern which has high intensities at 1.88 eV and nearly no intensity at 1.42 eV. In this case a $1s^2 2s 2p^6 3p$-$1s^2 2s 2p^6 3s$ coupling will be induced while the $1s^2 2s 2p^6 3p$-$1s^2 2s 2p^6 3d$ coupling is suppressed.

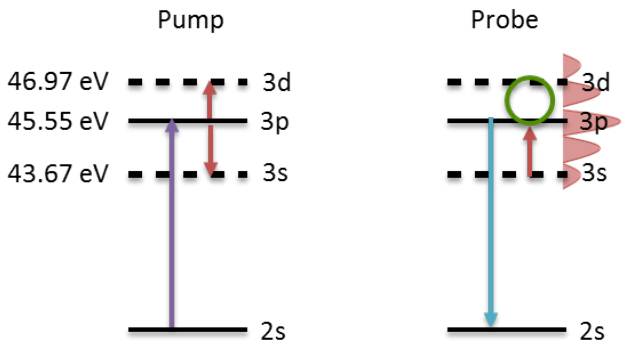

Figure 4.6.: Schematic drawing of the motivation for the following measured experiment. In the first step the XUV/NIR pump creates coherent superposition of the states $1s^2 2s 2p^6 3d$, $1s^2 2s 2p^6 3p$ and $1s^2 2s 2p^6 3s$. Due to the frequency-modulated NIR probe (spectrum drawn on the right) only one dark state is coupled to the $1s^2 2s 2p^6 3p$ state (red arrow), while the second coupling is not present (green circle). This should effect the dipole emission of the $1s^2 2s 2p^6 3p$ state (blue arrow).

4.3. NIR-NIR-XUV four-wave mixing experiment in neon

With the four-quadrant split-mirror it is now possible to generate multi-pulse sequences needed to obtain frequency modulated NIR light. Therefore the XUV/NIR pump pulse is reflected by one of the mirrors while the other two mirrors delay the two NIR pump pulses to generate the frequency modulation. Therefore the XUV light which was generated due to high harmonic generation in neon and the copropagating NIR beam are placed on the four-quadrant split-mirror in the way that the two upper mirrors contain a combination of XUV and NIR, while the two lower mirrors only contain NIR light. Since for this experiments only three light pulses are needed one of the upper mirrors is tilted that just one XUV/NIR pulse hits the target cell. The NIR frequency grating is therefore generated in a plane parallel to the laser table. Since for this experiment a combination of XUV and NIR light is used and the absolute value of the k vectors differ by a factor of about 30 ($k_{XUV} \gg k_{NIR}$) this experiment does not completely fulfill the boxcars geometry. Therefore the generated signal k_{signal} will not be deflected in k_4 direction and can not be measured background free. The measured signal will therefore be a combination of the signal from linear absorbtion and the FWM signal. To achieve a background free measurement for this pulse configuration one needs to increase the relative angle between the XUV/NIR pulses and the two NIR frequency pattern generating pulses.
The presented data was measured under the following experimental conditions: The XUV light for the measurements was produced in neon with a pressure of 195 mbar. The laser power was estimated as 2.8 W and the pulse length was given by 7.5 fs. Time delay scans were measured in neon with a target preassure of 44 mbar. Spectra were measured with an integration time of 1000 ms. The time t between the two NIR pulses was varied from 17.79 fs to -23.66 fs in 1.01 fs steps. The sign of t is only convention and indicates which of the two NIR pulses interacts first with the XUV/NIR light pulse. For each value of t time delay scans were carried out by varying T from -10fs to 65fs with a stepsize of 0.17 fs. A schematic drawing of the pulse configuration can be seen in figure 4.7. The two-color XUV/NIR pulse is printed in red and violet. The other two NIR pulses are shown in two different shades of red for a better visuality. For one time delay scan the time delay t between the two NIR is kept fixed while they were simultaneously scanned over the XUV/NIR pulse with the second time delay T.

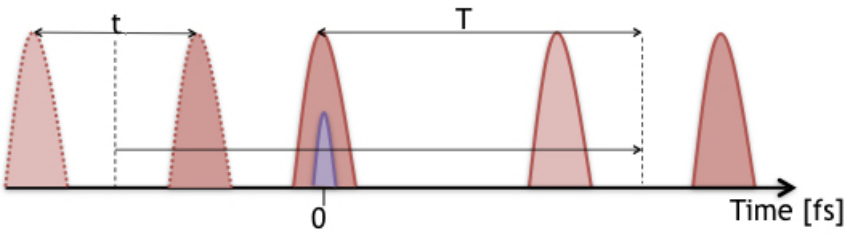

Figure 4.7.: Schematic drawing of the used pulse configuration. The delay t is used to change the produced spectral fringes. For each time delay t scans with varying T were measured. The center of the two NIR pulses is chosen as reference point for the varying time delay T in respect to the XUV/NIR excitation pulse, which is kept fixed at $T = 0$ fs.

Some selected time delay scans are presented in figure 4.8 and 4.9 (left) with their corresponding Fourier energy plots (right). In the presented energy range the resonance lines of neon for the transitions $2p^{-2}3s3p$, $2s^{-1}3p$, $2s^{-1}4p$ and $2s^{-1}5p$ can be seen. The corresponding Fourier energy plots are generated by Fourier transformation along the time delay axis T. For $t = 17.79$ fs an oscillation uppon the $2s^{-1}3p$ and $2s^{-1}4p$ resonance line can be seen at a time delay centered about $T = 50$ fs. For $t = 7.42$ fs an additionally oscillation appeares uppon the $2s^{-1}3p$ resonance line in the time delay plot for negative time delays T. For $t = 0.17$ fs this oscillation seems even stronger and additional the later oscillations are no longer centered at 50 fs but at 40 fs. Additional lineshape changes can not be clearly seen in this time delay scans. By observing the corresponding Fourier energy plots no big changes can be observed for the three cases. All three Fourier energy plots show contributions at about 1.7 eV Fourier energy for the $2s^{-1}3p$, $2s^{-1}4p$ and $2s^{-1}5p$ transitions, corresponding to the NIR photon energy. This is a link to the one-cycle NIR oscillation on the resonance lines which is an evidence for the 1-NIR dark state couplings between the bright and the dark states in neon. In the Fourier energy plot for $t = 0.17$ fs there is also a contribution of two times the NIR energy. This could come from a 2-NIR coupling between for example the $1s^2 2s 2p^6 3p$ and the $1s^2 2s 2p^6 4p$ states in neon since both NIR hit the target at the same time and no frequency modulation is generated for perfect temporal overlap between the two NIR pulses. While observing the three exemplary time delay scans for negative t one can observe that the oscillation at the $2s^{-1}3p$ resonance line for negative T and the oscillations upon the $2s^{-1}3p$, $2s^{-1}4p$ and $2s^{-1}5p$ resonance lines at positive T move towards each other. This effect could be based on the different $\mathbf{k_i}$ vectors and is quantified in the following. However there seems to be nearly no difference in the Fourier energy plots

for negative t.

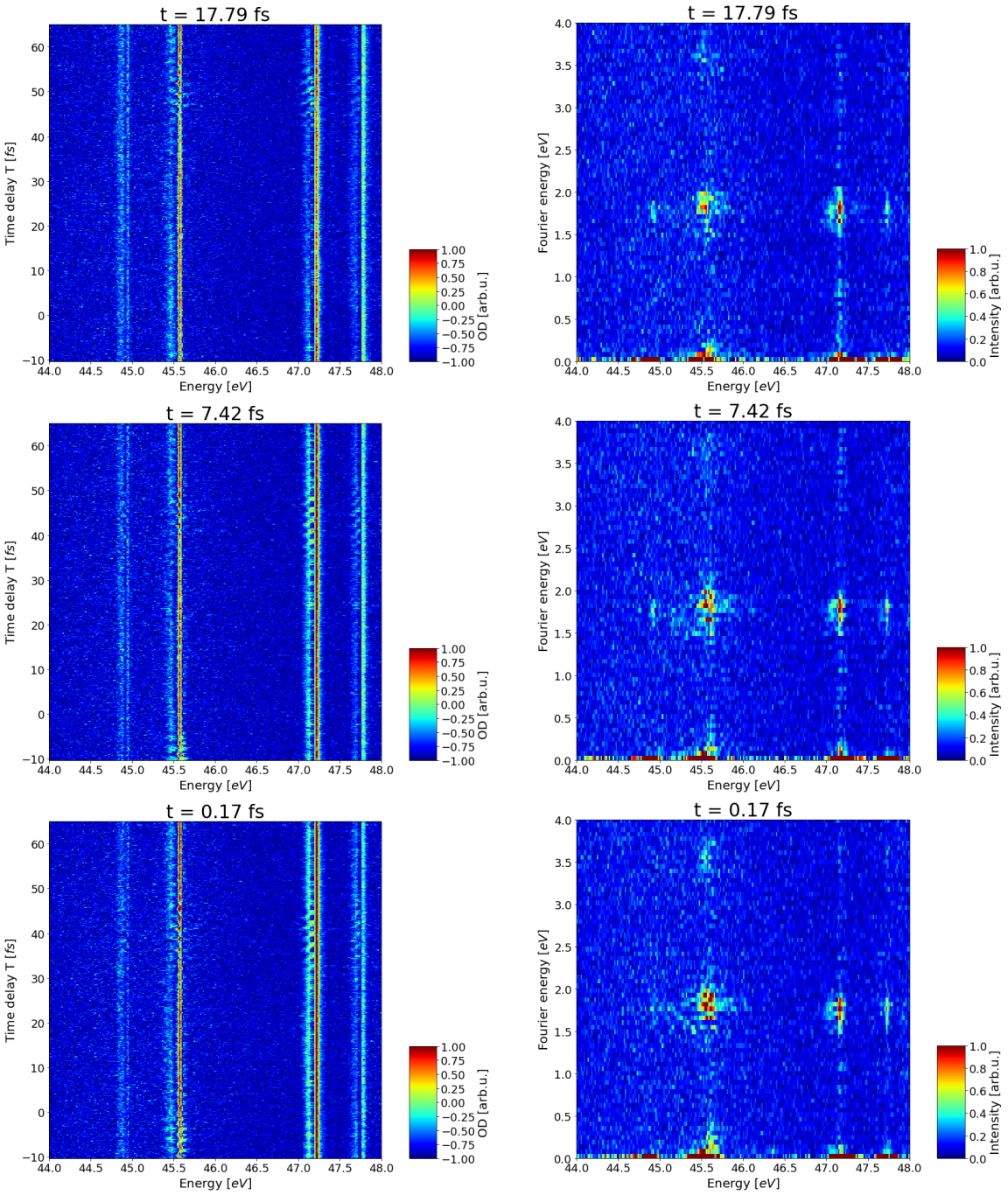

Figure 4.8.: Selection of measured time delay spectra with corresponding Fourier energy plots for positive t. In the presented energy range the resonance lines of neon for valence states $1s^2 2s^2 2p^4 3s3p$, $1s^2 2s2p^6 3p$, $1s^2 2s2p^6 4p$ and $1s^2 2s2p^6 5p$ can be seen. The Fourier energy plots are generated by Fourier transformation along the time delay axis T. All three Fourier energy plots show contributions at about 1.7 eV Fourier energy for the $1s^2 2s2p^6 3p$, $1s^2 2s2p^6 4p$ and $1s^2 2s2p^6 5p$ states, corresponding to the NIR photon energy. This is a link to the one-cycle NIR oscillation on the resonance lines which is an evidence for the 1-NIR dark state couplings between the bringht and the dark states in neon.

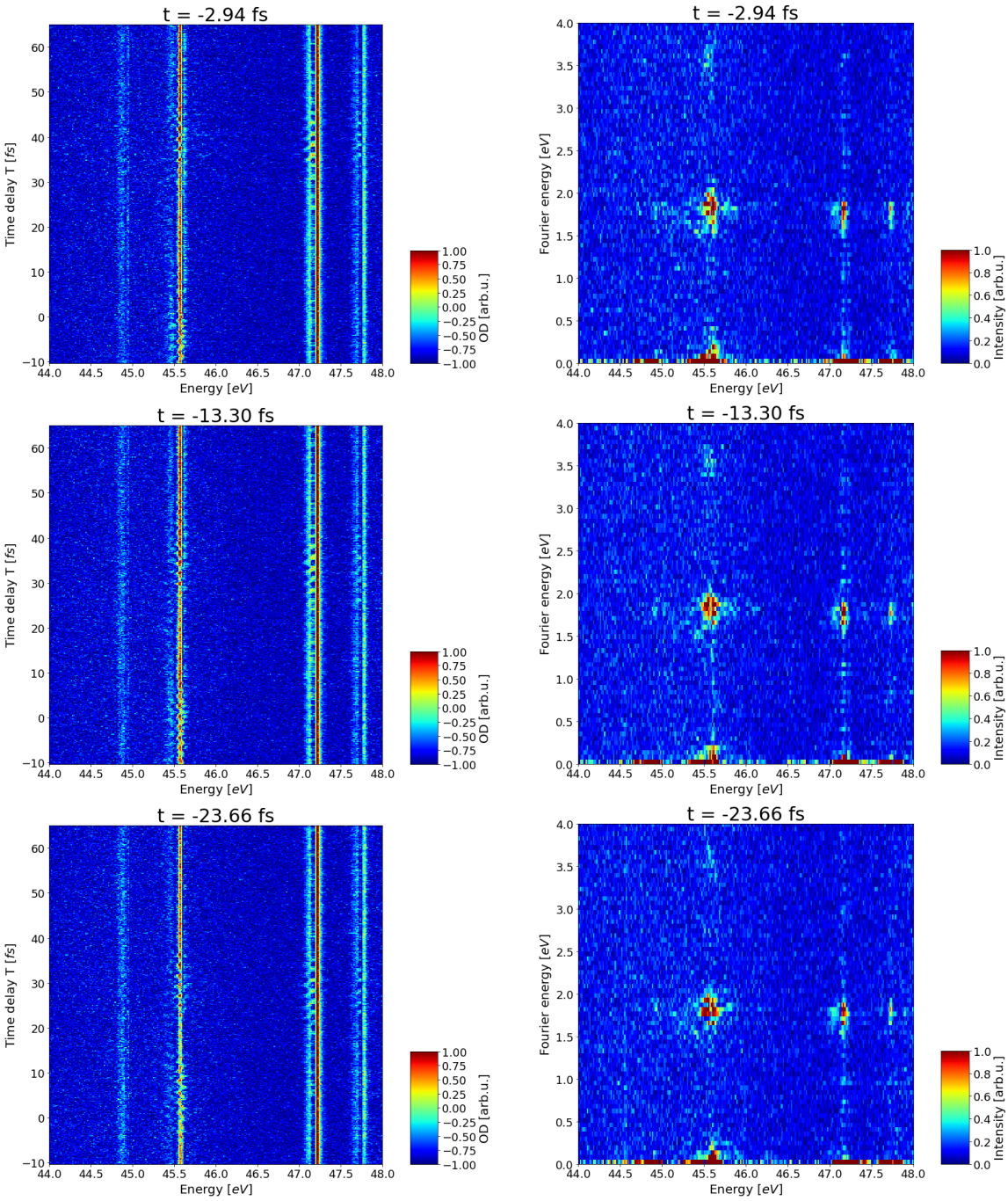

Figure 4.9.: Selection of measured time delay spectra with corresponding Fourier energy plots for negative t. In the presented time delay scans the resonance lines of neon for valence states $1s^2 2s^2 2p^4 3s3p$, $1s^2 2s2p^6 3p$, $1s^2 2s2p^6 4p$ and $1s^2 2s2p^6 5p$ can be seen. The corresponding Fourier energy plots are generated by Fourier transformation along the time delay axis T. Also the Fourier energy plots for negative t show contributions at about 1.7 eV Fourier energy. This is a link to the one-cycle NIR oscillation on the resonance lines which is an evidence for the 1-NIR dark state couplings between the bright and the dark states.

Since the measured data is very noisy and one wants to quantify the oscillations which are present on the neon $2s^{-1}3p$ resonance line, the data is Fourier filtered for Fourier energies between 1.6 eV and 2.0 eV. After selecting this Fourier energy range the data is Fourier transformed back into time domain. After the filtering process only the components with this oscillation frequencies appear in the time delay graphs and noise with other frequencies is filtered out. Also the resonance lines, which have Fourier energies at about 0 eV are therefore not present in the filtered data. In analogy to figure 4.8 and 4.9 six specific time delay scans are shown for only the selected frequencies. After Fourier filtering the oscillations at the position of the resonance lines can be clearly seen in figure 4.10 for the six selcected time delay scans. As can be seen for $t = 17.79$ fs the oscillation is present at all four depicted resonace line positions. With decreasing t the oscillation at negative time delays T moves towards positive T. For the time delay scan with $t = -23.66$ fs it even seems that a second oscillation at the energetic position of the $2s^{-1}4p$ resonance line appears. It has to be further investigated what would happen if t is decreased further. Unfortunately no values for $t < -23.66$ fs were measured. Another effect which can be observed is that for the first oscillation at the energetic position of $2s^{-1}3p$ resonace line no phase shift over the line can be observed, while for the second oscillation a phase shilft over the resonance line is present.

To quantify the two oscillations the spectral average of the energies from 45.50 eV to 45.65 eV was determined. As can be seen in figure 4.11 the spectral average contains three oscillations which vary in their form and position. To determine the position, phase and precise frequency a fit function according to

$$f(x) = \sum_{i=1}^{3} a_i \cdot \exp^{\frac{-(x-x_i)^2}{2w_i^2}} \cdot \sin(f_i \cdot x + c_i), \tag{4.3}$$

with amplitudes a_i, positions x_i, widths w_i, frequencies f_i and phases c_i, was used. The spectral averages and the corresponding fits can be seen in figure 4.11. As can be seen for the averaged spectra for the energies 45.50 eV to 45.65 eV a second oscillation appears due to averaging which was not observed in figure 4.10. It might be an artifact from averaging. Nevertheless it is fitted in the following for a better fit result for the other two oscillations. As can also be seen in figure 4.11 some fits appear to be conclusive (like $t = -2.94$ fs and $t = -13.30$ fs, while others are misleading (like $t = 17.79$ fs and $t = 7.42$ fs). To determine the exact change in the oscillations with respect to their position, phase and frequency and also to extract

misleading fits, the formula 4.3 is applied for all measured t.

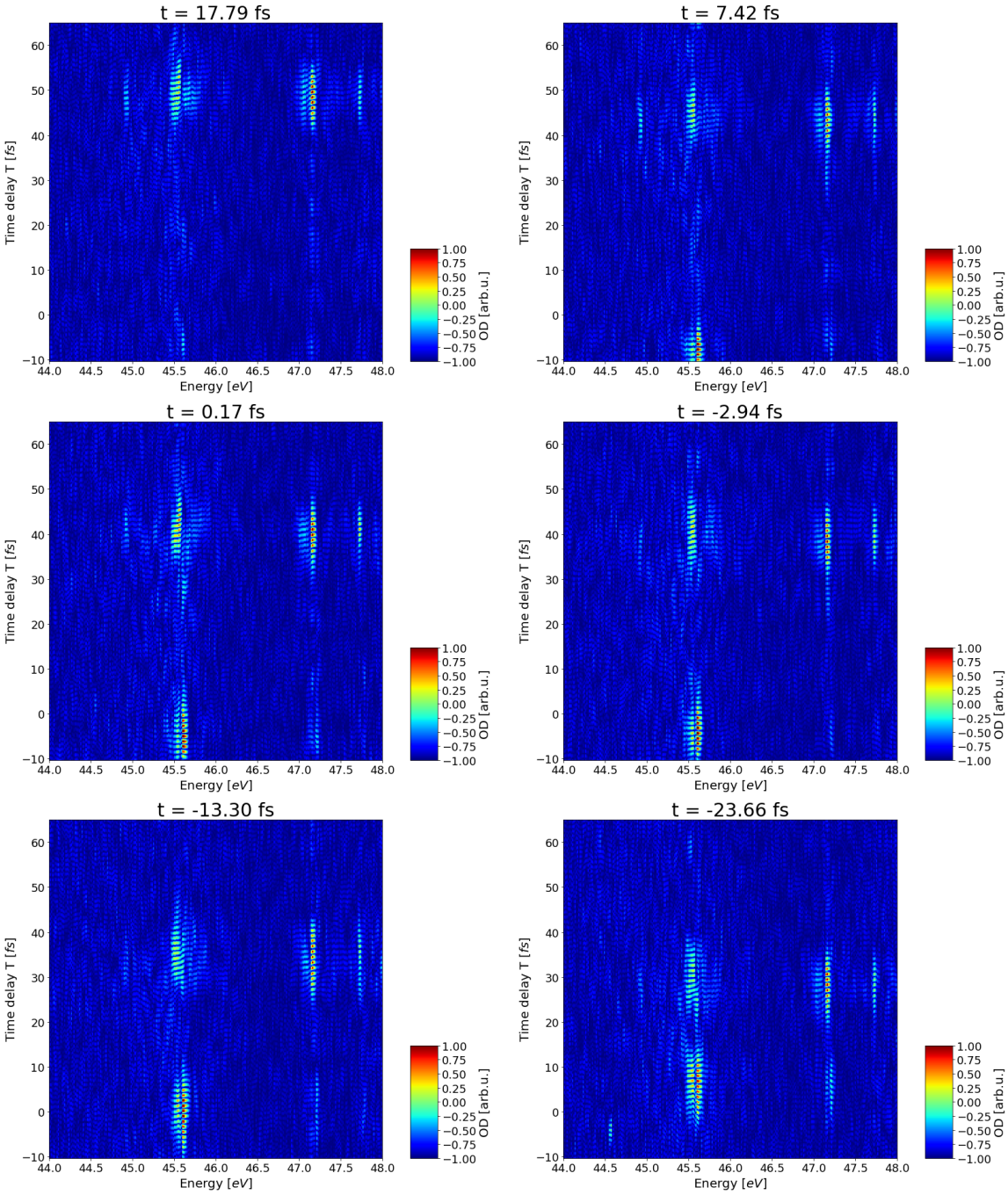

Figure 4.10.: Remaining oscillations after Fourier filtering of the Fourier energies between 1.6 eV and 2.0 eV. As can be clearly seen the two oscillations at the energetic position of the $2s^{-1}3p$ line move towards each other with decreasing t. Another effect which can be seen in the Fourier filtered time delay scans is that there is a phase shift over the resonance line for the oscillation at positive T, while no phase shift is observable for the first oscillation.

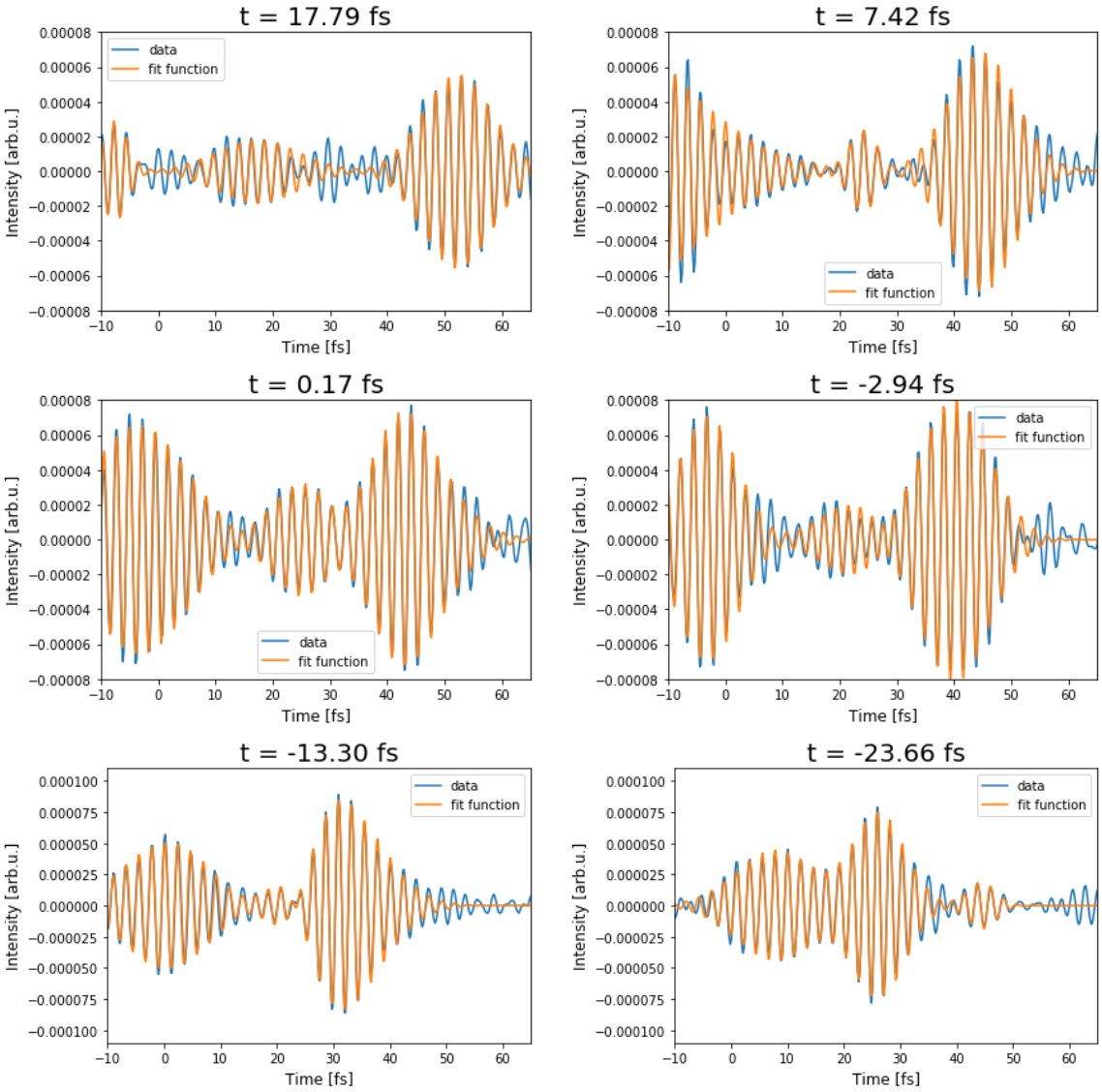

Figure 4.11.: Spectral average of the $2s^{-1}3p$ oscillations from figure 4.10 for the energy range 45.50 eV to 45.65 eV. The data is presented in blue and the fit according to equation 4.3 is shown in orange. As can be seen a second oscillation appears which was not observed in figure 4.10. It might be an artifact from averaging. Nevertheless it is fitted for a better fit result for the other two oscillations. The resulting fit parameters are plotted as a function of time delay t in figures 4.12 to 4.16.

Misleading fits result from the fact that fitting the first oscillation was often misleading since the oscillation was not completely on the measured time delay range T. Another reason was that for specific time delays t the first and second oscillations overlapped which also led to non-precise fits.

The determined fit parameter of equation 4.3 are then plotted for all t values. To get

a better impression of the behaviour of the fit paramters they are plotted in figures 4.12 to 4.16. For a first estimation the trend of all fit parameters is fitted by a linear fit according to

$$f(p_i) = A \cdot p_i + B, \tag{4.4}$$

with p_i being the parameter which should be fitted and coefficients A and B.
In figure 4.12 the oscillations amplitude a_i as a function of t, for the first (a_1) and the third oscillation (a_3) are plotted in blue. The fit line according to equation 4.4 is shown in orange. An oscillatory behaviour of the data points can be observed. This could be an indicator for the ability to turn off or on the NIR induced couplings between the bright $1s^2 2s 2p^6 3p$ and the dark states ($1s^2 2s 2p^6 3s$ and $1s^2 2s 2p^6 3d$). Therefore the strength of the coupling which is proportional to a should be maximal for the coupling with the two dark states, while it should be zero if no NIR coupling is induced. The linear fit for a_1 and a_3 led to the fit paramters:

$$A_{a_1} = (5.4 \pm 0.8) \cdot 10^{-5} \quad B_{a_1} = (1.3 \pm 0.7) \cdot 10^{-6} \tag{4.5}$$

$$A_{a_3} = (6.5 \pm 0.3) \cdot 10^{-5} \quad B_{a_3} = (-2.1 \pm 2.2) \cdot 10^{-9}. \tag{4.6}$$

Nontheless the measurement should be repeated with higher statistics to find a better fit function for the behaviour of the oscillation amplitudes a_i.

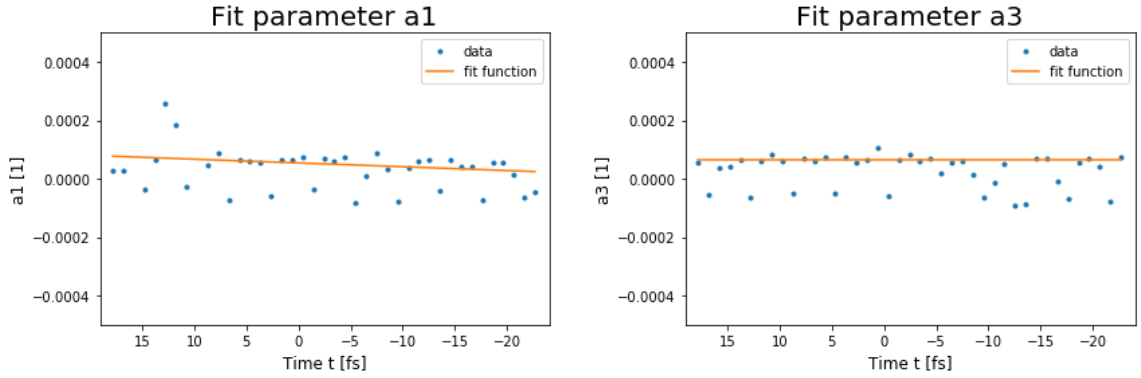

Figure 4.12.: Fit parameter a as a function of t, for the first (a_1) and the third oscillation (a_3). For first estimation the data points were fitted by a straight line. a_i should be big, if both dark states couple back to the $1s^2 2s 2p^6 3p$ bright state while it should be in extremal case zero if no NIR coupling between the bright and the dark states are induced. The fit results are presented in (4.5) and (4.6).

In figure 4.13 the fit paramter c, which represents the phase of the oscillation, is plotted as a function of t, for the first (c_1) and the third oscillation (c_3). As can be

seen the values for c_3 spread in a wide range. This is based on the fact that for the spectral average the signal was averaged over the phase shift. To get a better impression of the absolute phase value it sould be determined for both sides of the spectral line independently. The two linear fits for c_1 and c_3 led to the following values:

$$A_{c_1} = 3.19 \pm 0.17 \quad B_{c_1} = 0.02 \pm 0.01 \tag{4.7}$$

$$A_{c_3} = 8.17 \pm 0.32 \quad B_{c_3} = 0.08 \pm 0.03. \tag{4.8}$$

c_1 is therefore equal to π within the fit error, while c_3 equals to $\pi/2$ within the fit errors.

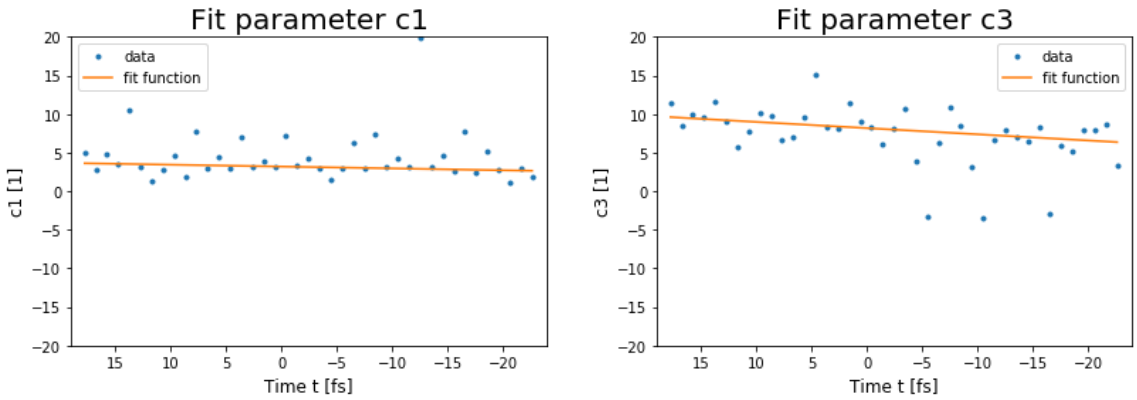

Figure 4.13.: Fit parameter c as a function of t, for the first (c_1) and the third oscillation (c_3). The parameter c describes the phase of the oscillation. For the first oscillation it is equal to π within the fit error while for the third oscillation the phase has a factor of $\pi/2$ within the fit error. As can be seen the values for c_3 spread in a wide range. This is based on the fact that vor the spectral average the signal was averaged over the phase shift. To get a better impression of the absolute phase value it sould be determined for both sides of the spectral line independently.

In figure 4.14 the fit parameter f, which represents the frequency of the oscillation is shown as a function of t, for the first (f_1) and the third oscillation (f_3). As can be seen both frequencies stayed constant during the complete experiment. It would be also interesting to repeat the experiment with more statistics and to find out if both oscillation frequencies are the same or if they only differ because of the small fit

errors. The linear fit revealed following parameters for the oscillation frequencies:

$$A_{f_1} = (2.80 \pm 0.01)\frac{1}{fs} \qquad B_{f_1} = (12 \pm 7) \cdot 10^{-4} \tag{4.9}$$

$$A_{f_3} = (2.76 \pm 0.01)\frac{1}{fs} \quad B_{f_3} = (0.2 \pm 4.2) \cdot 10^{-4}. \tag{4.10}$$

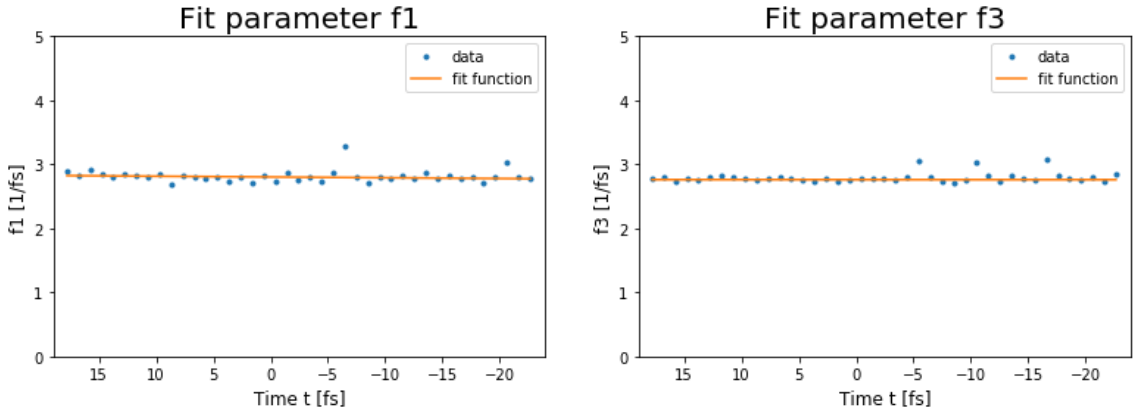

Figure 4.14.: Fit parameter f as a function of t, for the first (f_1) and the third oscillation (f_3). The frequency of both oscillations seems to stay constant during the 2D experiment. It could be interesting to repeat the experiment with more statistics to verify, if the frequencies f_1 and f_2 are equal. Since for this fit the calculated error is so small f_1 and f_2 are not equal with in the errors estimated.

The fit parameter w (which describes the width of the oscillation) is shown as a function of t, for the first (w_1) and the third oscillation (w_3) in figure 4.15. As can be seen w_1 spreads over a range of 40 fs. This comes from the fact that fitting the first oscillation was often misleading since the oscillation was not completely on the measured time delay range T. Another reason is that during the evaluation the first and second oscillation overlaped for specific t which also led to a non-precise fit for this quantity. Regardless the absolute value of w_3 stays constant which means that the third oscillation mantains its temporal width independent of the used NIR pulse configuration. The fit parameters are given by:

$$A_{w_1} = (5.0 \pm 1.2)fs \quad B_{w_1} = -0.03 \pm 0.10 \tag{4.11}$$

$$A_{w_3} = (6.7 \pm 0.2)fs \quad B_{w_3} = 0.02 \pm 0.02. \tag{4.12}$$

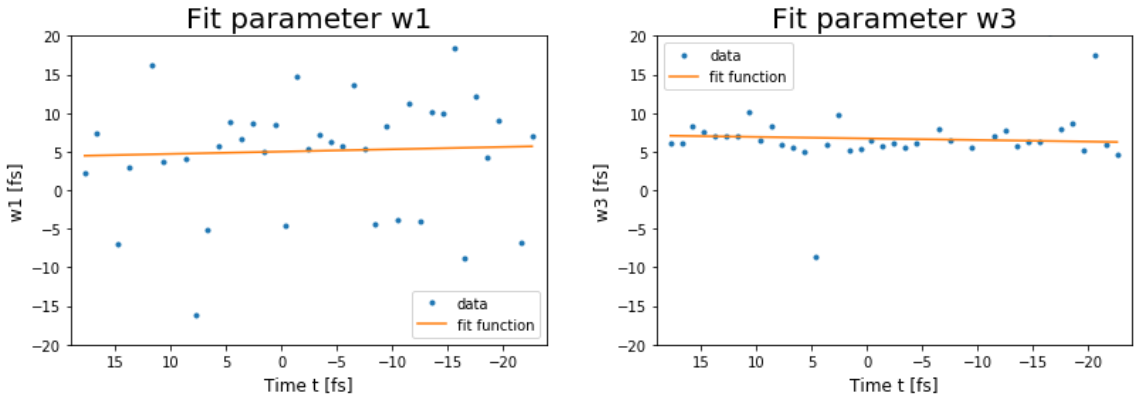

Figure 4.15.: Fit parameter w as a function of t, for the first (w_1) and the third oscillation (w_3). The width w_1 of the first oscillation spreads over a range of 40 fs. This comes from the fact that fitting the first oscillation was often misleading since the oscillation was not completely on the measured time delay range T or due to evaluation the first and second oscillation overlaped which also led to a non-precise fit for this quantity. In comparison the absolute value of w_3 stayed constant which means that the third oscillation mantains its temporal width independent of the used NIR pulse configuration.

The remaining parameter to fit is the position of the oscillation x for the first (x_1) and the third oscillation (x_3). The most obvious change in the measured data is the displacement of the two oscillatons as a function of the NIR pulse spacing t, which seems to have a linear behaviour. As can be seen in figure 4.16, x_1 increases for decreasing t, while the temporal position x_3 decreases with decreasing time t. To quantify the amount of displacement the linear fit is appropriate. It results in:

$$A_{x_1} = (-2.9 \pm 0.6)fs \quad B_{x_1} = -0.42 \pm 0.05 \tag{4.13}$$

$$A_{x_3} = (41.4 \pm 0.2)fs \quad B_{x_3} = 0.53 \pm 0.02. \tag{4.14}$$

The two oscillations move towards each other by 1 fs, if the distance between the two NIR pulses is decreased by 1fs.

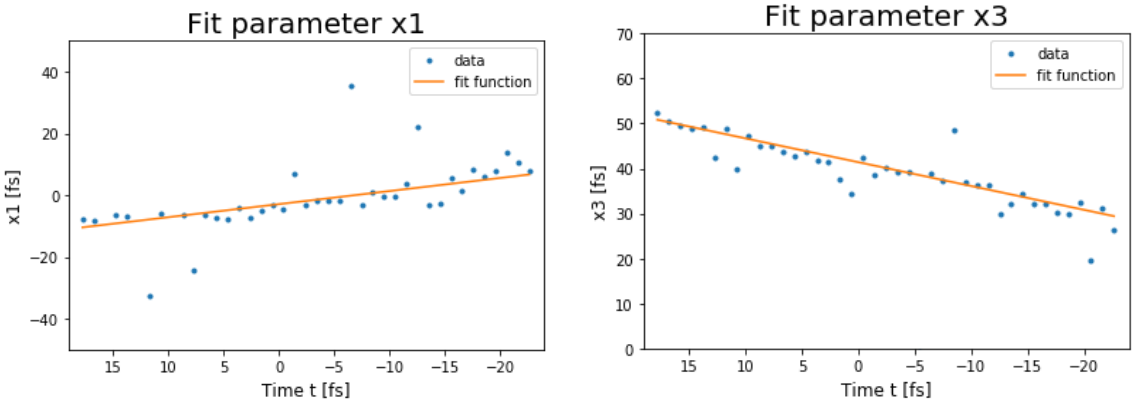

Figure 4.16.: Fit parameter x as a function of t, for the first (x_1) and the third oscillation (x_3). The most obvious change in the measured data is the displacement of the two oscillatons as a function of the NIR pulse spacing t, which has a linear behaviour. The position x_1 of oscillation 1 increases for decreasing t, while for the third oscillation the temporal position decreases with decreasing time t.

5. All-XUV four-wave mixing experiments in neon at FLASH

5.1. Instrumental setup for SASE-FEL experiments

The experimental X-MuSIC setup was modified for the SASE-FEL experiments at FLASH. The major differences will be explained in the following. Since it is only allowed to use the FLASH end stations with ultra-high vacuum (UHV) conditions (and our experiments require target gas pressures of several tens of mbar) we used additonal differential pumping in this setup to improve the gas pressure. Two of the pumping station chambers were provided with apertures to fix the beam position and to generate a spatially well-defined FEL beam. Since for the SASE-FEL experiments the FEL was the only light source used, the complete HHG chamber was removed for this setup. This means that after the pumping stations the mirror chamber is the first chamber to come. The mirror chamber has been completely redesigned for the beamtime at FLASH. The main reason for this was the reduction of the grazing incidence angle from 15 to 8 degrees to improve in XUV-light reflectivity. Since under the smaller angle the focal spot on the optics increases in the horizontal direction, the before used gold coated mirrors were not long enough. For this purpose new optics were used and also the coating was changed from gold to carbon, since carbon has a smaller surface roughness and a 10 percent higher reflectivity in the used XUV spectral region than gold. To further improve reflectivity and focussing, the toroidal mirror was exchanged by an ellipsoidal mirror with the imaging property 80:1. This was chosen because the FEL source has a distance of roughly 80 meters to the ellipsoidal mirror. Therefore the FEL source is reproduced in the target cell. Since the ellipsoidal mirror and also the split mirrors need to be longer due to the grazing incidence angle of 8 degrees, a new mirror chamber was designed. In the wake of this development also a cluster flange was designed which allows to simultaneously measure the mirror stability during the experimental runs. Therefore a laser can be

shined upon the mirror under a different angle for simultaneous stability measurements without effecting the experiment. After the four-quadrant split-mirror a variable 2D-slit is placed inside the mirror chamber which allows to block each fragment of the split mirror individually. In the next vacuum chamber several boxcars-masks are installed with variable hole sizes and distances to create the for this experiment desired boxcars geometry. The now clearly separated and round beams propagate through the target cell and are blocked in the next chamber by the second 2D-slit to only measure the created signal in the $\mathbf{k_4}$ direction (see figure 2.7) on the CCD camera chip. The created signal propagates through the spectrometer which was not changed for the SASE-FEL experiments and is measured on the CCD camera chip.

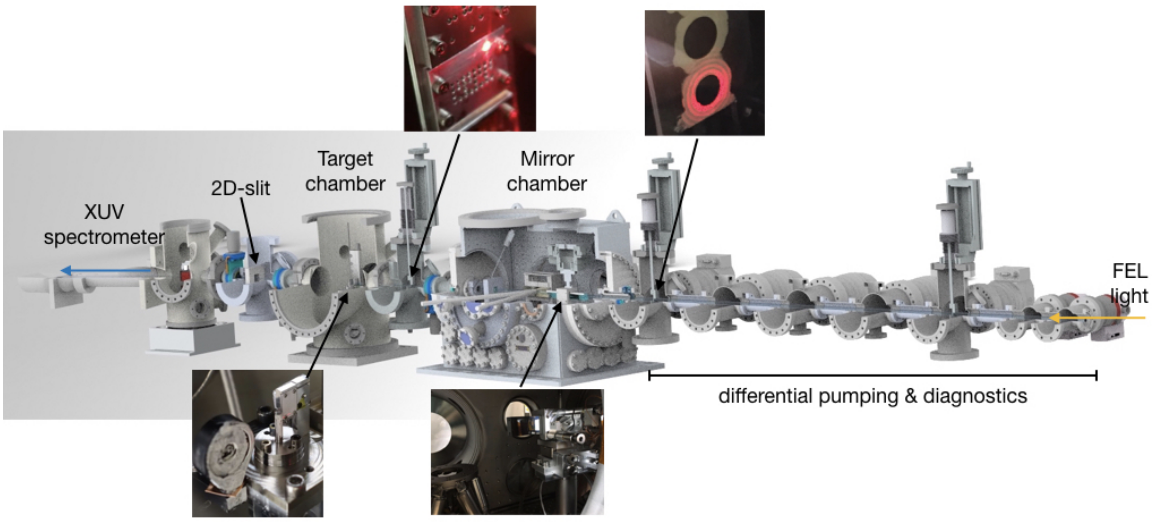

Figure 5.1.: Sketch of the X-MuSIC beamline for SASE-FEL experiments. The FEL light (yellow arrow) propagates from the right to the left through the experimental setup. The first seven chambers have the aim to improve gas pressure due to differential pumping. Two of them are equipped with apertures to fix the beam position and to generate a well-defined spatial beam. Afterwards the beam propagates through the mirror chamber where it is focussed and split into four parts. These four parts pass through a boxcars mask in the next chamber to generate four well-defined spatial beams. The beams then hit the target cell in the next chamber. Since the expected FWM signal is weak in comparison to the generating fields, all beams apart from the signal are blocked in the next chamber with a motorized 2D-slit. Therefore only the signal hits the spectrometer and is measued on the XUV detector. Details from inside the chambers can be seen in the photographs. The black arrows mark the locations in the chambers.

5.2. Specific setup stability

Since the experimental setup changed for the SASE-FEL experiments it is necessary to measure the stability again for this specific setup. One major change which could influence the stability is the fact that this setup is not built on top of a laser table but on an ITEM frame. At the same time an improvement in mirror stability is expected due to the reduction of the grazing incidence angle to 8 degrees.
For the stability measuremts at FLASH the beamline-internal adjustment laser (Schäfter + Kirchhoff diode laser) was used to measure the stability. Analogous to the stability measurements in the laboratory the two beams were coupled out of the beamline and measured in the spatial overlap of the two foci with a CMOS camera. The evaluation scheme for the non-normalized and normalized data kept unchanged.

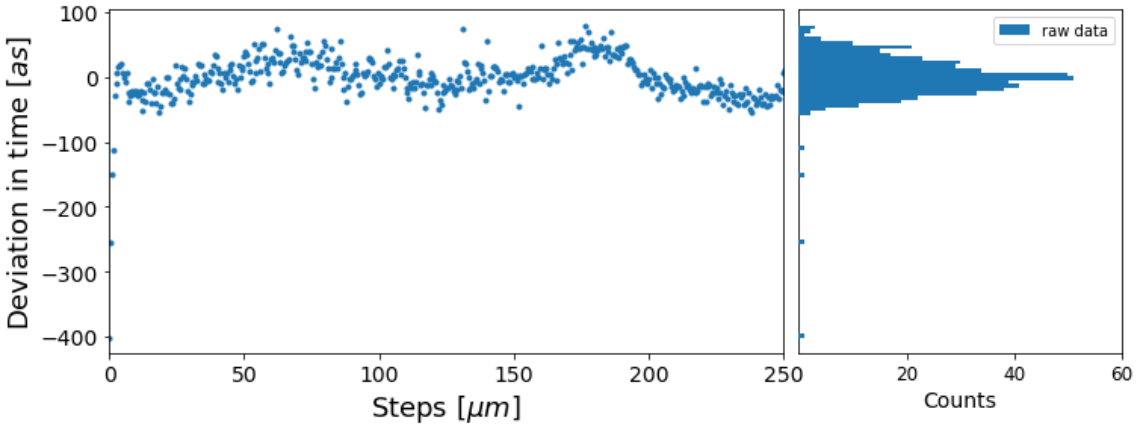

Figure 5.2.: Left: measured deviation in time as function of the delay steps, right: binned histogram over the entire step range.

As can be seen in figure 5.2 it seems that the measured temporal fluctuations have a slight oscillation imprinted, which could come from the vibrations in the supporting ITEM frame in comparision to the monolithic laser tables. The large deviation of the first 5 data points stems from the Fourier filtering of the DC components and are neglected as outliers in the following. The fit for the corresponding histogram in figure 5.3 reveals a standard deviation of 26.1 as in comparison to the standard deviation of 43.0 as which was measured on the HHG setup (see figure 3.5).
As expected the stability for the four-quadrant split-mirror in the SASE-FEL setup is better which is mainly due to the smaller grazing incidence angle of 8 degrees. The conversion from μm to fs changes to

$$1\mu m = 0.928 fs. \tag{5.1}$$

As can be seen in figure 5.3 on the right-hand side, the normalized histogram contains less total counts than the non-normalized one. The reason for this is that since the laser clips at the edges of the CMOS chip during the measurement, not the entire delay range was considered for the evaluation since not the complete beam profile was on the chip. This decreases the total number of counts. Due to limited beam time it was not possible to repeat this measurement at FLASH. The non-normalized stability is a sum of several contributions which also include vibrations from the turbo pumps and the item frame. So for a rough estimation of the mirror stability the non-normalized stability should be taken into account.

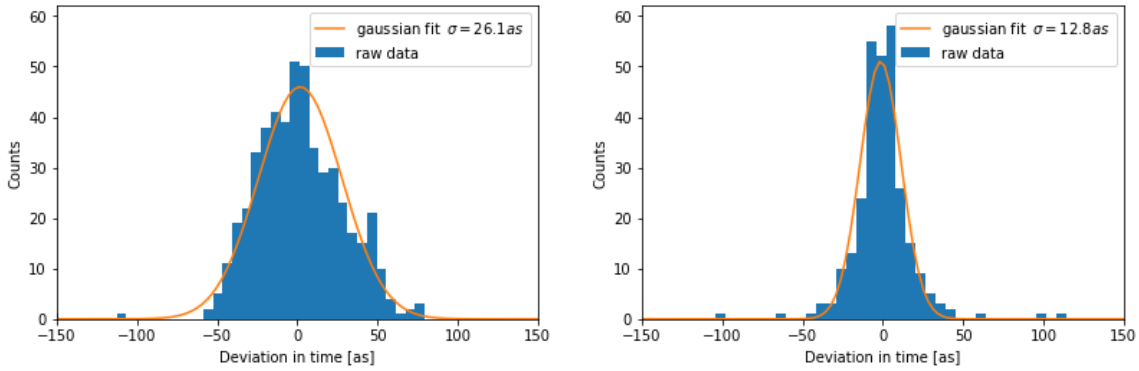

Figure 5.3.: Histograms and fits for the stability measurement for the SASE-FEL setup. On the left the non-normalized histogram in blue with corresponding fit in orange (stability of 26.1 as) and on the right the normalized histogram (stability of 12.8 as) for the same data set. As can be easily seen the normalization leads to an improvement in stability of more than 50 percent.

5.3. Boxcars-mask and preliminary data

The designed boxcars mask can be seen in figure 5.4. The drill hole size used was $d_a = 1$ mm and the distance between two respectives holes was choosen as $d_h = 1.3$ mm. The mask itself has a variation of possibilities to be used. During the experiment the configuration in the middle of the bottom row is used, so that for first tests the local oscillator keeps blocked. Given the FEL wavelength $\lambda \approx 25$ nm, the hole distance d_h and the respective distance between the boxcars-mask and the target

gas d_t, the fringe line spacing of the generated grating in the target gas can be estimated analogous to Young's double slit experiment:

$$y = \frac{\lambda}{\theta} = \frac{\lambda \cdot d_t}{d_h} = 5.15 \mu m. \tag{5.2}$$

Since the focus of the FEL light in the target was about 10 μm the generated transient grating only consists of 2-3 grating lines.

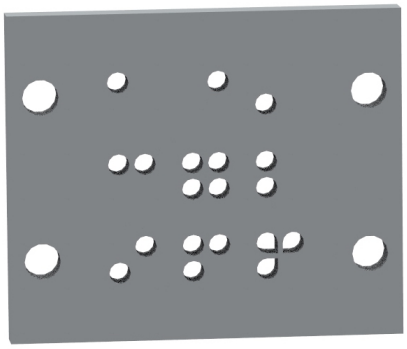

Figure 5.4.: CAD drawing of designed boxcars mask for four-wave mixing experiments. For the experiments the configuration in the middle of the bottom row was used.

An advantage of all-XUV four-wave mixing experiments in comparison to NIR-NIR-XUV FWM is the fact that the absolute value of the wave vectors is equal. Therefore it is possible to carry out the experiment under perfect boxcars condition and measure a FWM signal in $\mathbf{k_4}$ direction which is background free. In this work first FWM data will be presented as a proof-of-principle for FWM experiments and is not in the scope of this work.
The data presented in the following was taken with neon as a target gas. The pressure applied on the target cell was about 35 mbar and the signal was measured in 1st diffraction order as single-shot full-chip images (with 10 ms integration time each). For the presented data 10000 single-shot images were averaged. Figure 5.5 shows the measured signal as a function of the position on the CCD camera. For this image the local oscillator was blocked directly after the split-mirror while the other three beams which generated the signal were blocked after the target with the second 2D-slit. To make sure that the generated FWM signal is free of stray light of the three generating beams full-chip images were taken with only two beams hitting the target. Since three beams are necessary to generate a FWM signal in this case only the stray

light should be visible without a FWM signal. For this case two beams were blocked by the first 2D-slit directly after the split-mirror and the other two were led through the target. The stray light was measured for all combinations and averaged. It can be seen in figure 5.6. To get only the FWM signal without stray light the data of 5.6 was substracted from 5.5. The resulting signal can be seen in 5.7.

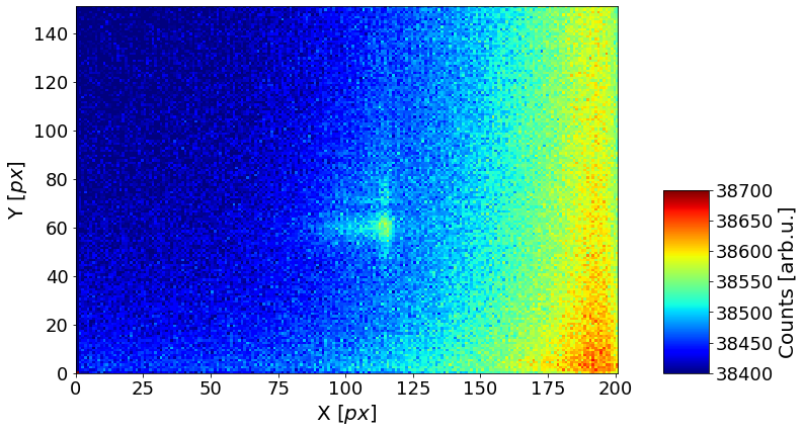

Figure 5.5.: Measured FWM signal in 1st diffraction order. This data contains the generated FWM signal as well as remaining stray light from the three generating pulses.

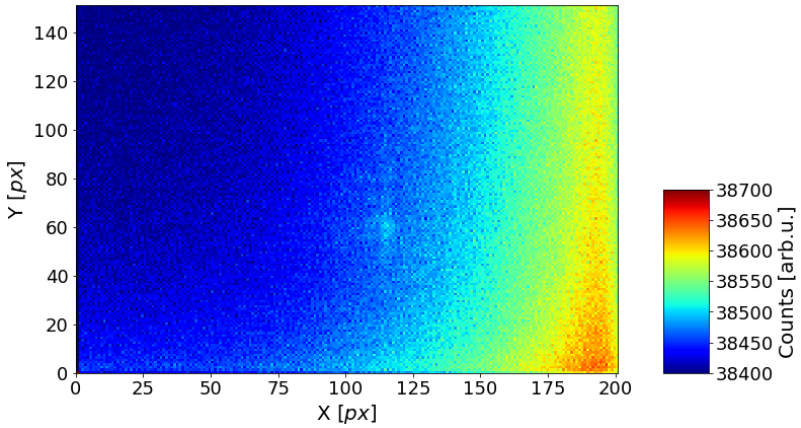

Figure 5.6.: Sum of all stray light components. To determine only the stray light only two beams were let through the target cell. In this case no FWM in this direction should be generated. All combinations of two beams were measured and averaged for this figure.

Figure 5.7 can be seen as a proof-of-principle that first FWM experiments with a FEL light source and the split-mirror are possible. To further quantize the measured signal it is necessary to investigate how the signal changes with FEL intensity and target gas pressure.

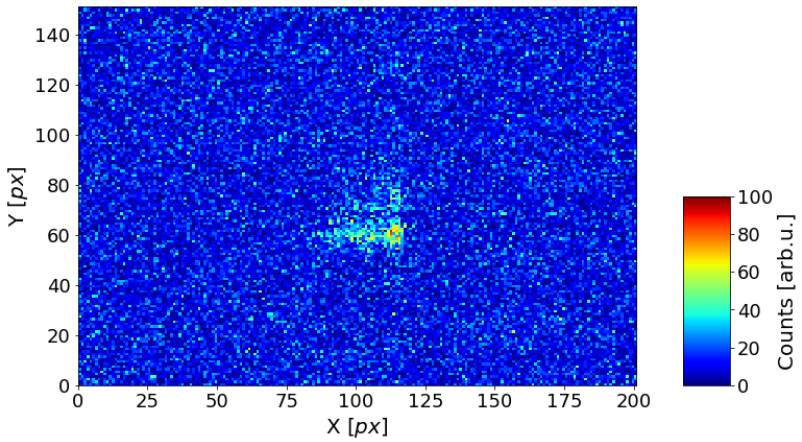

Figure 5.7.: Solely the FWM signal in 1st diffraction order without stray light from the incident beams. To get more information about the measured signal other data sets need to be evaluated.

6. Conclusion

The aim of this work was to quantify whether FWM experiments in the XUV spectral regime could be performed with the existing X-MuSIC beamline using a four-quadrant split-mirror. The mirror has the ability to split an incident beam into four identical copies to perform four-wave mixing experiments. For this purpose the stability of the split-mirror was determined with an inteferometric setup using a HeNe laser.
From this measurements the deduction was drawn that the four-quadrant split-mirror can only be used with the needed precision, if the hexapod positioner it is mounted on is turned off. Therefore it was possible to achieve a temporal stability of $\sigma_t = 12.8$ as. Also the temporal overlap between the respective mirrors was determined with a linear autocorrelation measurement carried out with a Ti:Sa laser.
Since the X-MuSIC setup was designed for the use with HHG sources as well as for free-electron lasers, first measurements haven been carried out at both light sources. These measurements were presented and evaluated in this thesis.
The measurement with the high-harmonic light source presented in this work contained therefore one XUV/NIR beam and additional two NIR beams to generate a modulated NIR spectra. By changing the modulation frequency, by delaying the two NIR pulses with respect to each other, it was observed if it is possible to specifically adress the $2s^{-1}3p$ resonance to the close-by 3s and 3d states in neon. Futhermore first all-XUV four-wave mixing experiments in neon have been carried out at the free-electron laser facility FLASH in Hamburg.
These measurements confirm the ability of the four-quadrant split-mirror to perform FWM experiments in the XUV spectral range and serve as a next step to future four-wave mixing experiments in the XUV spectral region.

Bibliography

[1] W. P. Aue, E. Bartholdi, and R. R. Ernst. Two-dimensional spectroscopy. Application to nuclear magnetic resonance. *The Journal of Chemical Physics*, 64(5):2229–2246, 1976.

[2] Nicolaas Bloembergen. Nonlinear optics and spectroscopy. *Reviews of Modern Physics*, 54:685–695, 1982.

[3] N. A. Kurnit, I. D. Abella, and S.R. Hartmann. Observation of a Photon Echo. *Physical Review Letters*, 13(19):567–569, 1964.

[4] E J Brown, Q G Zhang, and M Dantus. Femtosecond transient-grating techniques: Population and coherence dynamics involving ground and excited states. *Journal of Chemical Physics*, 110(12):5772–5788, 1999.

[5] Shaul Mukamel. Multidimensional Femtosecond Correlation Spectroscopies of Electronic and Vibrational Excitations. *Annu. Rev. Phys. Chem.*, 51:691–729, 2000.

[6] John C. Wright. Multiresonant Coherent Multidimensional Spectroscopy. *Annual Review of Physical Chemistry*, 62(1):209–230, 2011.

[7] Yizhu Zhang, Kristina Meyer, Christian Ott, and Thomas Pfeifer. Passively phase-stable, monolithic, all-reflective two-dimensional electronic spectroscopy based on a four-quadrant mirror. *Optics Letters*, 38(3):356–358, 2013.

[8] Thomas Ding, Christian Ott, Andreas Kaldun, Alexander Blättermann, Kristina Meyer, Veit Stooss, Marc Rebholz, Paul Birk, Maximilian Hartmann, Andrew Brown, Hugo Van Der Hart, and Thomas Pfeifer. Time-resolved four-wave-mixing spectroscopy for inner-valence transitions. *Opt. Lett.*, 41(4):709–712, Feb 2016.

[9] B.E.A. Saleh and M. C. Teich. *Fundamentals of Photonics*. John Wiley & Sons, Inc., 2003.

[10] H. Beutler. Über Absorptionsserien von Argon, Krypton und Xenon zu Termen zwischen den beiden Ionisierungsgrenzen 2p 3/2 und 2p 1/2. *Zeitschrift für Physik*, 93:177–196, 1934.

[11] Ugo Fano. Sullo spettro di assorbimento dei gas nobili presso il limite dello spettro d'arco. *Il Nuovo Cimento (1924-1942)*, 12(3):154–161, Mar 1935.

[12] U. Fano. Effects of Configuration Interaction on Intensities and Phase Shifts. *Physical Review*, 124(6):1866–1878, 1961.

[13] C. Ott, A. Kaldun, P. Raith, K. Meyer, M. Laux, J. Evers, C. H. Keitel, C. H. Greene, and T. Pfeifer. Lorentz Meets Fano in Spectral Line Shapes: A Universal Phase and Its Laser Control. *Science*, 340(6133):716–720, 2013.

[14] Thomas Ding. *Quantum dynamics in weak and strong fields measured by XUV nonlinear spectroscopy*. PhD thesis, 2018.

[15] M Schultze, M Fieß, N Karpowicz, J Gagnon, M Korbman, M Hofstetter, S Neppl, A L Cavalieri, Y Komninos, Th Mercouris, C A Nicolaides, R Pazourek, S Nagele, J Feist, J Burgdörfer, A M Azzeer, R Ernstorfer, R Kienberger, U Kleineberg, E Goulielmakis, F Krausz, and V S Yakovlev. Delay in Photoemission. *Science*, 328:1658–1662, 2010.

[16] K T Taylor, M A Lysaght, L A A Nikolopoulos, and J S Parker. The RMT method for many-electron atomic systems in intense short-pulse laser light. *Journal of Modern Optics*, 58:1132–1140, 2011.

[17] L R Moore, M A Lysaght, J S Parker, H W Van Der Hart, and K T Taylor. Time delay between photoemission from the 2 p and 2 s subshells of neon. *Physical Review A*, 84(061404), 2011.

[18] K Codling, R P Madden, and D L Ederer. Resonances in the Photo-Ionization Continuum of Ne I (20-150 eV). *Physical Review*, 155:26–37, 1967.

[19] Konrad Schulz, Michael Domke, Ralph Pu, Gregory Miecznik, and Chris H Greene. High-resolution experimental and theoretical study of singly and doubly excited resonances in ground-state photoionization of neon. *Physical Review A*, 54:3095–3112, 1996.

[20] G Min, Z Lin-Fan, L Cun-Ding, and X Ke-Zun. Optically Forbidden Excitations of 2s Electron of Neon Studied by Fast Electron Impact. *Chinese Physics Letters*, 25(3646), 2008.

[21] D Spence. Autoionising states of Ne in the energy range 41 to 52 eV derived from near-threshold scattered- electron spectra. *Journal of Physics B: Atomic and Molecular Physics*, 14:129–147, 1981.

[22] Shaul Mukamel. *Principles of Nonlinear Optical Spectroscopy*. Oxford University Press, Inc., 1995.

[23] P. B. Corkum. Plasma Perspective on Strong-Field Multiphoton Ionization. *Physical Review Letters*, 71(13):1994–1997, 1993.

[24] Deutsches-Elektronen-Synchrotron. Free-electron laser FLASH. https://flash.desy.de/, (accessed January 26, 2018).

[25] Zhirong Huang and Kwang-Je Kim. Review of x-ray free-electron laser theory. *Phys. Rev. ST Accel. Beams*, 10:034801, Mar 2007.

Part I.

Appendix

A. Acknowledgements

At this point I would like to thank all members of the Interatto/X-MuSIC group for the friendly working atmosphere and the amount of knowledge shared with me.
Special thanks goes to:
Prof. Dr. Thomas Pfeifer who welcomed me, first as an intern later as a master's student, to the Interatto/X-MuSIC group and gave me the opportunity to work in the ultrafast community.
Priv. Doz. Robert Moshammer for being the second reviewer and all the laughter during my first beamtime at FLASH.
Dr. Christian Ott for supervising me, the discussions and for the big input during data evaluation.
Marc Rebholz - without him this thesis would not be as it is. I thank him for introducing me to the to the experimental setup, for answering all my questions, proof reading of this work and his patience.
Lennart Aufleger for the Labview skills he taught me.
Maximilian Hartmann for the encouraging talks, his open ear and also for the help while struggeling with Python.
Dr. Thomas Ding for sharing his knowlegde and experience.
Patrick Rupprecht for sharing his experience concerning optics and his critical point of view.
Alexander Magunia for all the joint coffee breaks.
Paul Birk for answering my questions concerning stability measurements.
Veit Stoß and **Gergana Borisova** who always had an open ear.
Dr. Martin Laux and **Dr. Alexander Blättermann** for easing working life at the table soccer.
Last but not least I would like to thank my parents. Without their on-going trust and support I wouldn't even had the opportunity to study at all.

B. Deposition

Erklärung:

Ich versichere, dass ich diese Arbeit selbstständig verfasst habe und keine anderen als die angegebenen Quellen und Hilfsmittel benutzt habe.

Heidelberg, den 01. Februar 2018 .....